

Oriented secondary magnetite micro-inclusions in plagioclase from oceanic gabbro

GE BIAN^{1,*}, OLGA AGEEVA^{1,2,†}, VLADIMIR RODDATIS³, GERLINDE HABLER¹, ANJA SCHREIBER³, AND RAINER ABART¹

¹University of Vienna, Department of Lithospheric Research, Josef-Holaubek-Platz 2, 1090 Vienna, Austria

²Institute of Geology of Ore Deposits, Petrography, Mineralogy, and Geochemistry (IGEM), Staromonetnyi 35, Moscow 119017, Russia

³Helmholtz Centre Potsdam, GFZ German Research Centre for Geosciences, Telegrafenberg, D-14473, Potsdam, Germany

ABSTRACT

Plagioclase-hosted submicrometer to micrometer-sized oriented needle- and lath-shaped magnetite micro-inclusions with their elongation direction aligned parallel to the plagioclase [001] (PL[001]) direction were investigated using correlated optical, scanning electron, and scanning transmission electron microscopy. The PL[001] magnetite micro-inclusions formed from older generations of differently oriented magnetite micro-inclusions by recrystallization during hydrothermal alteration. Six orientation variants of PL[001] magnetite micro-inclusions occur, and they share the same shape orientation but differ in their crystallographic orientation relationships to the plagioclase host. The magnetite-plagioclase interfaces are faceted. High-resolution scanning transmission electron microscopy revealed that interface facets are aligned parallel to low-index lattice planes corresponding to oxygen layers of either magnetite or plagioclase. In addition, the linkage between prominent crystal structure elements of magnetite and plagioclase across the interfaces and accommodation mechanisms minimizing misfit between the two crystal structures were discerned. Combined evidence suggests that the shape and shape orientation, as well as the crystallographic orientation relationships between the magnetite micro-inclusions and the plagioclase host, are crystallographically controlled. The close crystal-structural link between magnetite precipitates and plagioclase host ensures a low-energy configuration driving recrystallization of older generations of differently orientated magnetite micro-inclusions into those that are aligned parallel to PL[001] and facilitates the underlying reaction kinetics. Due to their single to pseudo-single domain characteristics, the plagioclase-hosted magnetite micro-inclusions are particularly robust carriers of natural remanent magnetization. Recrystallization of differently oriented preexisting magnetite micro-inclusions into magnetite micro-inclusions with uniform shape orientation parallel to PL[001] has interesting consequences for the magnetic anisotropy of magnetite-bearing plagioclase grains.

Keywords: Plagioclase-hosted magnetite micro-inclusions, crystal and shape orientation relationships, interface facets, scanning transmission electron microscopy, crystallographic control

INTRODUCTION


Plagioclase (PL) from mafic plutonic rocks frequently contains needle-, lath- and plate-shaped magnetite (MT) micro-inclusions (Wager and Mitchell 1951; Davis 1981; Feinberg et al. 2006b; Selkin et al. 2014; Ageeva et al. 2016, 2020; Cheadle and Gee 2017). The inclusions typically show systematic crystallographic orientation relationships (CORs) and shape orientation relationships (SORs) to the plagioclase host (Sobolev 1990; Ageeva et al. 2020). For needle- and lath-shaped magnetite micro-inclusions, two basic orientation types are discerned. The first type is represented by the so-called “plane-normal” type inclusions, which are elongated parallel to one of their MT<111> directions and are aligned parallel to the normal direction of specific plagioclase lattice planes. The second inclusion type is elongated along one of the MT<110> directions, which is aligned parallel to the PL[001] direction. The magnetite inclusions of

the plane-normal type are probably formed by precipitation from Fe-bearing plagioclase during late magmatic stages (Bian et al. 2021). The MT {222} planes correspond to densely packed oxygen layers in the crystal structure of magnetite, and they are aligned with plagioclase lattice planes corresponding to oxygen layers in the crystal structure of plagioclase, indicating that a good fit between the oxygen sublattices of the two phases represents the basis of the observed orientation relationships of the plane normal type inclusions (Ageeva et al. 2020). The “PL[001] type” micro-inclusions typically occur in the outermost regions of the plagioclase grains, and they are the dominant micro-inclusion type in samples that experienced hydrothermal overprint at sub-solidus conditions (Pertsev et al. 2015). The PL[001] type magnetite micro-inclusions are thus ascribed to hydrothermal processes (Ageeva et al. 2022). PL[001] type magnetite micro-inclusions have also been described from metamorphic rocks (Feinberg et al. 2004; Wenk et al. 2011).

Magnetite is the most important carrier of rock magnetism, and the systematic SORs of the magnetite micro-inclusions with the plagioclase host lead to the magnetic anisotropy of

* E-mail: bian9@gmx.at

† Orcid 0000-0002-0158-2749

 Open access: Article available to all readers online. This article is CC-BY.

magnetite-bearing plagioclase. This is of interest in the context of paleomagnetic reconstructions because due to their size, the magnetite micro-inclusions typically have single-domain or pseudo-single-domain magnetic characteristics, which makes them particularly robust carriers of remanent magnetization (Kent et al. 1978; Fleet et al. 1980; Davis 1981; Dunlop and Özdemir 2001; Renne et al. 2002; Feinberg et al. 2006a; Knafelc et al. 2019). The magnetic anisotropy arising from their anisotropic shape orientation distribution may, however, bias their magnetic record. In particular, the vector of natural remanent magnetization obtained from a magnetite-bearing plagioclase grain may deviate from the direction of the magnetic field prevailing at the time when the rock cooled through the Curie temperature (Usui et al. 2015; Nikolaisen et al. 2022), an effect that needs to be accounted for during paleomagnetic reconstructions. It was argued by Ageeva et al. (2022) that the orientation distribution of the needle- and lath-shaped magnetite micro-inclusions undergoes an evolution from an initial dominance of the plane-normal types, which prevail in pristine magmatic plagioclase, toward a dominance of the PL[001] type inclusions in hydrothermally overprinted feldspar. Such a shift in inclusion populations has important implications for the magnetic memory of magnetite-bearing plagioclase grains.

Oriented micro-inclusions of magnetite in clinopyroxene, of hematite in rutile (Hwang et al. 2010), and of rutile in garnet (Hwang et al. 2000, 2015, 2019; Proyer et al. 2013) have been studied using conventional transmission electron microscopy (TEM), and the crystallographic and shape orientation relationships between the inclusions and the host crystals have been rationalized based on TEM results. Through the advent of spherical aberration-corrected scanning transmission electron microscopy (STEM) (Haider et al. 1998; Krivanek et al. 1999; Pennycook 2017), atomic-scale imaging of silicate minerals has become possible (Kogure and Okunishi 2010), offering unprecedented insight into the crystal structure and interfaces in crystalline materials (Li et al. 2016).

In this study, we made use of these developments and investigated PL[001] type magnetite micro-inclusions. The morphology, the spatial distribution, the CORs and SORs of PL[001]-MT type micro-inclusions with respect to the plagioclase host as well as the microscopic configurations of the magnetite-plagioclase interfaces were analyzed using correlated microscopy covering phenomena from the micrometer to the nanometer scale. More specifically, optical microscopy, including universal stage, scanning electron microscopy (SEM), which includes electron backscatter diffraction (EBSD), and scanning transmission electron microscopy (STEM), were combined. Interface facet orientations were rationalized based on geometrical models of the microscopic configurations at magnetite-plagioclase interfaces, and the evolution from plane-normal type to the PL[001] type inclusions was addressed.

MATERIALS AND METHODS

Materials

Magnetite-bearing plagioclase grains from oceanic gabbro samples 277-10s-d4, 277-10-d23, and 277-7-d12 were studied. The samples were dredged from the ocean floor during the 30th cruise of the Research Vessel Professor Logachev (Beltenev et al. 2007, 2009). The dredge sites were located in an oceanic core complex along

the Mid-Atlantic Ridge at 13°N (Karson and Lawrence 1997; MacLeod et al. 2009). Detailed geological descriptions of the region can be found in MacLeod et al. (2009); Ondráš et al. (2012); Pertsev et al. (2012), and Escartin et al. (2017). The studied samples were taken from coarse-grained gabbro mainly comprised of plagioclase, clinopyroxene, orthopyroxene, and amphibole. In a petrographic thin section, oriented needle-, lath-, and plate-shaped micro-inclusions of an opaque phase are observed in plagioclase.

Methods

Scanning electron microscopy. Secondary electron (SE) imaging and electron backscattered diffraction (EBSD) analyses of plagioclase hosting magnetite micro-inclusions were performed on an FEI Quanta 3D FEG-SEM, located at the Faculty of Earth Science, Geography and Astronomy, University of Vienna, Austria. The SEM is equipped with a Schottky-type field-emission electron gun and an EDAX Pegasus Apex IV detector system comprising an EDAX Digiview V EBSD camera for crystallographic orientation determination. SE imaging was performed on chemo-mechanically polished carbon-coated thin sections. During EBSD analysis and secondary electron imaging, the electron beam was set to an accelerating voltage of 15 kV and a probe current of ca. 4 nA in analytical mode. The stage was at 70° tilt, and the working distance was in the range of 14–14.5 mm. Details of the analytical parameters during EBSD analysis are described in Ageeva et al. (2022, Section 2.4 therein). SE imaging was performed at 70° stage tilt and tilt-corrected. An about ±1° error in the tilting angle may exist due to the uneven surface of the thin section, which may introduce errors in the tilt correction and cause up to 1.3° error in the determination of the directions of interface traces.

Focused ion beam and Ar ion-milling. STEM specimens were prepared by Ga-FIB and Ar ion-milling. Specimen 277-10-d23 was extracted by focused ion beam (FIB) nanomachining using the FEI Quanta 3D FEG instrument described above. The ion column is equipped with a liquid Ga-ion source, a gas injection system for Pt and C deposition, and an Omniprobe 100.7 micromanipulator for in situ lift-out. Based on combined EBSD crystal orientation data and optical microscopy, a site and orientation-specific TEM foil of a PL[001]-MT needle cross section was prepared from a chemo-mechanically polished carbon-coated thin section. In a first step, a platinum layer was deposited at the extraction site to protect and support the TEM foil. The FIB section was oriented exactly perpendicular to the elongation direction of a PL[001]-MT inclusion. During FIB preparation, SE imaging was used for monitoring progress. The electron beam settings were at 15 kV accelerating voltage and ca. 53 pA probe current. The setting for FIB-induced SE imaging was 30 kV accelerating voltage and 10 pA probe current. For FIB nanomachining, an accelerating voltage of 30 kV was applied. During the extraction process, successively decreasing FIB probe current with 65, 30, 5, and 1 nA was used. Then, Pt-deposition at FIB settings of 30 kV and 0.1 nA was used to attach the TEM foil first to the tip of a tungsten micromanipulator needle and subsequently for mounting the foil to a Mo grid. The extracted TEM foil was about 20 × 20 μm in size and about 1.6 μm thick. Further thinning was done by subsequent Ar ion-milling.

A second TEM specimen was prepared from sample 277-7-d12 using a FEI Helios G4 UC Dual Beam (SEM-FIB). The instrument is located at Deutsches GeoForschungsZentrum (GFZ), Potsdam Imaging and Spectral Analysis (PISA) facility. To this end, a cylinder of 3.1 mm diameter and 2 mm height was extracted from a 2 mm thick rock chip. The cylinder was then polished to produce a 100 μm thick circular disk. The disk contains a single-plagioclase grain with abundant magnetite micro-inclusions of different types. Final thinning of the disk was done using a Gatan DuoMill 600 instrument, operated at a voltage of 1 kV using argon ions (Ar⁺) at an incident angle of 15° to remove residual amorphous material. In the TEM foil prepared from the rock chip, the identity of the investigated inclusions was not known a priori but had to be determined from the STEM experiments a posteriori.

Scanning transmission electron microscopy. A Thermo Fisher Scientific Themis Z 3.1 transmission electron microscope was used for high-resolution imaging of the magnetite-plagioclase interfaces. The instrument is located at GFZ, PISA facility. The microscope is equipped with a Cs S-CORR probe corrector (spatial resolution at 300 kV < 0.06 nm) and a SuperX detector for energy-dispersive X-ray spectroscopy (EDS) to perform chemical analysis. High-angle annular dark-field (HAADF) and integrated differential phase contrast (iDPC) images were collected using STEM-HAADF and DF4 detectors using an accelerating voltage of 300 kV and a current of 10 pA. The convergence semi-angle of the incident probe was set to 30 mrad.

The iDPC-STEM method enables direct imaging of the phase of the transmission function for non-magnetic samples (Lazić et al. 2016). For thin samples, this yields an image that is directly interpretable as the (projected) electrostatic potential (Yücelen et al. 2018). There are several advantages to using the iDPC-STEM. (1)

It is capable of imaging light and heavy elements simultaneously at sub-angstrom resolution with a low-dose incident beam. (2) HAADF and iDPC images can be collected simultaneously. And (3) the signal-to-noise ratio (SNR) is superior to annular dark-field (ADF) STEM imaging and also to other high-resolution phase contrast techniques (Yücelen et al. 2018). In our study we collected both HAADF and iDPC images for all analyzed magnetite needles and facets simultaneously. We also collected annular bright-field ABF-STEM images at conditions usually used for visualizing oxygen atomic columns, see e.g., Jin et al. (2016). Online Materials! Figure S1 shows HAADF, ADF, and iDPC-STEM images of plagioclase collected from the same area, and corresponding simulated images obtained from QSTEM software are inserted for comparison (Koch 2002). Online Materials! Figure S1 demonstrates that all images, including iDPC, indeed can be directly interpreted, meaning that the bright or dark spots correspond to the positions of atomic columns.

RESULTS

Petrography

The investigated gabbro samples are mainly comprised of plagioclase, which is present at about 50% by volume, together with clinopyroxene, orthopyroxene, and amphibole, each of which is present at about 10 to 15 vol%. Plagioclase has a grain size of about 1 to 3 mm and anorthite contents of 40 to 60 mol%, where the cores usually have higher anorthite contents than the rims. The lowest anorthite contents are observed along healed cracks, which probably were formed during hydrothermal stages. Plagioclase shows twinning after the Albite, the Pericline, and the Carlsbad twin laws and contains abundant oriented micrometer and submicrometer-sized needle- and lath-shaped inclusions of an opaque phase, which is mainly magnetite. In addition, plate-shaped magnetite micro-inclusions are present. Typically, the needle and lath-shaped magnetite micro-inclusions are absent in the immediate vicinity of the plate-shaped inclusions. Finally, magnetite nano-inclusions with equant shapes are present, which are referred to as “dust-like inclusions.” Some of the magnetite micro-inclusions contain lamellar or irregularly shaped precipitates of ilmenite and/or ulvöspinel.

For needle- and lath-shaped magnetite micro-inclusions, seven SORs with respect to plagioclase are discerned that define the “plane-normal” type inclusions according to the terminology of Ageeva et al. (2022). These inclusions are elongated parallel to one of their $MT\langle 111 \rangle$ directions, and they are aligned close to parallel to the normal direction of one of seven specific plagioclase lattice planes, including $PL(112)_n$, $PL(1\bar{5}0)_n$, $PL(\bar{3}12)_n$, $PL(150)_n$, $PL(100)_n$, $PL(1\bar{1}2)_n$, and $PL(\bar{3}\bar{1}2)_n$, where $PL(hkl)_n$ is the direction normal to the $PL(hkl)$ lattice plane. One additional inclusion type is elongated along one of the $MT\langle 110 \rangle$ directions, which is aligned parallel to the $PL[001]$ direction. Henceforth, these inclusions are referred to as “ $PL[001]$ inclusions.”

Figure 1a shows the distribution of the different inclusion types in a grain of magmatic plagioclase in plane-polarized transmitted light. The plagioclase contains abundant oriented magnetite inclusions. Only in an irregularly “star-shaped” domain are the magnetite micro-inclusions absent, and the plagioclase appears bleached. In the central regions of the bleached domain, large equant grains of ilmenite are present, which appear to have collectively recrystallized from the pre-existing plane-normal type magnetite micro-inclusions and will not be further addressed in this study. In the domains furthest away from the bleached inclusion-free area magnetite micro-inclusions of the plane normal type dominate, corresponding to domains of pristine magmatic plagioclase (right-hand side of Fig. 1a). At

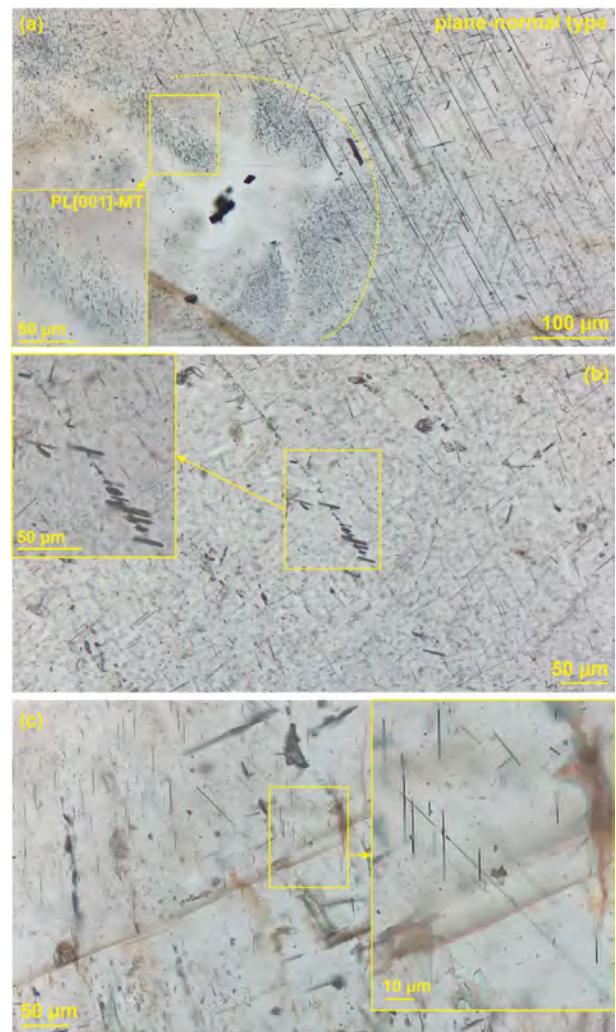


FIGURE 1. Plane-polarized transmitted light optical images of plagioclase with abundant oriented magnetite micro-inclusions. (a) Irregularly shaped bleached domain with large isometric opaque Fe-Ti oxide (ilmenite) inclusions in the central regions surrounded by a halo (delimited by dashed yellow line) with dominantly fine-grained $PL[001]$ type magnetite micro-inclusions and plane normal type inclusions outside the halo. A closeup of a domain with abundant $PL[001]$ type inclusions (yellow rectangle) is shown in the insert on the lower left. (b) Array of lath shaped $PL[001]$ -MT micro-inclusions along a thin healed crack, a closeup is shown in the insert. (c) $PL[001]$ -MT micro-inclusions (vertical) growing on a pre-existing plane-normal type magnetite micro-inclusion, a closeup is shown in the insert.

the transition between the pristine and the bleached domains, $PL[001]$ inclusions dominate (dashed yellow lines in Fig. 1a). According to Bian et al. (2021), the magnetite micro-inclusions of the plane-normal type probably formed by precipitation from Fe-bearing plagioclase, which had become supersaturated with respect to magnetite during late magmatic stages. The ilmenite plates in the central regions of the bleached domains and the $PL[001]$ inclusions are clearly of secondary, likely of hydrothermal origin. A more localized situation is shown in Figure

1b. There, several lath-shaped PL[001]-MT type inclusions are aligned along a straight line interpreted as a healed crack. In this case, recrystallization of the plane normal type magnetite micro-inclusions into PL[001]-MT inclusion was confined to the healed crack itself, whereas plane-normal type magnetite micro-inclusions dominate around the healed crack. Another situation corroborating the secondary nature of the PL[001] inclusions is shown in Figure 1c. There several PL[001] inclusions grew on a pre-existing plane-normal type inclusion.

CORs of PL[001]-MT micro-inclusions

PL[001]-MT micro-inclusions typically have prismatic shape. Combining crystal orientation data and universal stage measurements the elongation direction of type PL[001]-MT inclusions are found to be aligned with the PL[001] direction to within the accuracy of the universal stage optical measurements, which is about $\pm 3^\circ$. EBSD based crystal orientation analysis showed that the needle- and lath-shaped PL[001]-MT micro-inclusions are elongated parallel to one of their MT<110> directions and that their COR to the plagioclase host is characterized by the parallel alignment of PL[001] \parallel MT<110> to within the accuracy of the orientation determination by Hough-transform based EBSD analysis, which is at $< 1^\circ$ orientation deviation. Some of the dust-like inclusions show an approximate alignment of one of their MT<110> directions with the PL[001] direction with an angular deviation of about 5° between the two directions. Nevertheless, these dust-like inclusions are classified as PL[001] type inclusions.

Given the parallel alignment of the PL[001] and one of the MT<110> directions, additional crystallographic alignments between magnetite and plagioclase define three orientation variants of PL[001] type inclusions, which are referred to as orientation variants COR1A, COR1B, and COR2, each of which has two subgroups due to the presence of two magnetite twins. Specific Miller indices are applied for describing these CORs, and the conventions for assigning crystallographic directions are listed in Table 1. All three CORs have in common the parallel alignment of the crystallographic PL[001] and MT[110] directions to within $\sim 5^\circ$, as specified in row 1 of Table 1. The three orientation variants are discerned based on the additional parallel alignment of one of the MT{111} planes with specific lattice planes of plagioclase, as indicated in row 3 of Table 1. COR1A with PL(150) \parallel MT(1 $\bar{1}$ 1) and COR1B with PL(1 $\bar{5}$ 0) \parallel MT(1 $\bar{1}$ 1) are very closely related to one another, and typically form prismatic micro-inclusions. In contrast, COR2 with PL(120) \parallel MT(1 $\bar{1}$ 1) is different and typically forms dust-like inclusions. The two crystallographic alignments imply a third crystallographic alignment related to one of the MT<001> directions, which is described in row 2 of Table 1. It must be noted that the

MT{111} planes are twin planes associated with the spinel twin law, a 180° rotation about the plane normal to the MT{111} twin plane. As a consequence, for the CORs defined by the entries in rows 1–3 of Table 1 with respect to one twin variant of magnetite, another set of rational CORs exists with respect to the other twin variant of magnetite. Thus, for each of the three orientation variants, two subgroups exist, one with rational CORs with respect to magnetite twin 1 and another one with rational CORs with respect to magnetite twin 2. The second subgroup is defined by the alignment of PL[001] \parallel MT[110] for COR1A and by PL[001] \parallel MT[1 $\bar{1}$ 0] for COR1B and COR2, as listed in row 4 of Table 1, in addition to the alignments parallel to the twin plane as indicated in row 3 of Table 1. The third crystallographic alignment that follows naturally for the second subgroup is given in row 5 of Table 1. The CORs listed in rows 3–5 of Table 1 define the second subgroup with respect to magnetite twin 2 for each of the three COR variants. Thus, a total of six orientation variants exist for the PL[001] type inclusions, which are all characterized by rational CORs between the PL[001]-MT micro-inclusions and the plagioclase host.

The structural and orientation correspondences between magnetite and plagioclase with COR1A are illustrated in Figure 2. Figure 2a shows the plagioclase crystal structure with PL[$\bar{1}4,10,-7$], PL(150), and PL(1 $\bar{5}$ 0) indicated. A projection of the plagioclase unit cell along PL[001] is shown in Figure 2b. Figures 2c and 2d show the magnetite crystal structure according to COR1A with magnetite twin 1 and twin 2, respectively, and with MT[001], MT(1 $\bar{1}$ 1), and MT(1 $\bar{1}$ 0) indicated. The correspondence between plagioclase and magnetite lattice planes and lattice directions is highlighted by corresponding color codes. Figure 2e shows a projection of the two magnetite twins in COR1A. The same illustrations as given for COR1A in Figure 2, are given for COR1B in Figure 3. A simplified sketch of the orientation correspondence between the plagioclase and magnetite unit cells in COR1A and COR1B is shown in the Online Materials¹ Figure S2.

Interface orientations

In cross section, the prismatic PL[001]-MT type inclusions have convex polygonal shape comprised of pairs of parallel straight traces corresponding to different segments of a faceted inclusion-host interface. Secondary electron (SE) images of COR1A PL[001]-MT micro-inclusions pertaining to magnetite twin 2 are shown in Figure 4 together with a stereographic projection illustrating the COR between the magnetite inclusions and the plagioclase host. All inclusions shown in Figure 4 are hosted in a single-crystal domain of plagioclase with uniform crystallographic orientation. It is seen from the stereographic projection in Figure 4a that one of the MT<110> directions

TABLE 1. COR variants of PL[001]-MT micro-inclusions

	COR1A	COR1B	COR2	Row no.
Magnetite twin 1	PL[001] \parallel MT(1 $\bar{1}$ 0) PL[14,10,7] \sim \parallel MT[001]	PL[$\bar{1}4,10,-7$] \parallel MT[001] PL[001] \sim \parallel MT[110]	PL[001] \parallel MT[110] PL[023] \parallel MT[010]	1 2
Magnetite twin plane	PL(150) \parallel MT(1 $\bar{1}$ 1)	PL(150) \parallel MT(1 $\bar{1}$ 1)	PL(120) \parallel MT(1 $\bar{1}$ 1)	3
Magnetite twin 2	PL[001] \parallel MT[110] PL(150) \parallel MT(1 $\bar{1}$ 0)	PL(1 $\bar{5}$ 0) \parallel MT(1 $\bar{1}$ 0) PL[001] \sim \parallel MT[1 $\bar{1}$ 0]	PL[001] \parallel MT[1 $\bar{1}$ 0] PL(1 $\bar{2}$ 0) \parallel MT(1 $\bar{1}$ 3)	4 5
Inclusions shape	Mostly prismatic	Mostly prismatic	Mostly dust-like	6

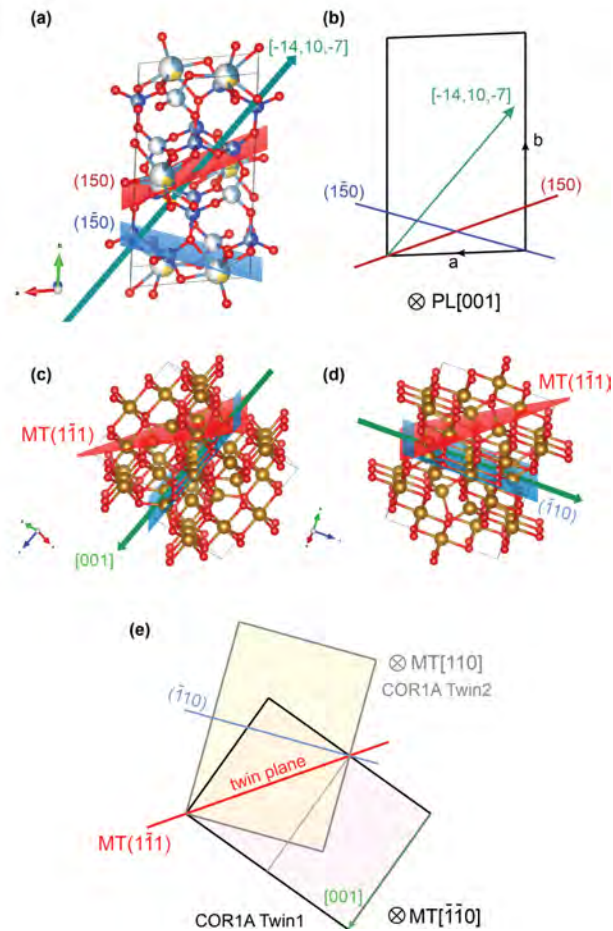


FIGURE 2. (a) Crystal structure model of plagioclase with $PL[-14,10,-7]$, $PL(150)$, and $PL(150)$ indicated. (b) 2D projection of the plagioclase unit cell viewing direction $\parallel PL[001]$ with $PL[-14,10,-7]$, $PL(150)$ and $PL(150)$ indicated. (c) Crystal structure model of magnetite with $MT(111)$, $MT(111)$ and $MT(110)$ indicated and with magnetite in the orientation of COR1A twin 1, i.e., $PL[001] \parallel MT[\bar{1}\bar{1}0]$, $PL[-14,10,\bar{7}] \parallel MT[001]$, and $PL(150) \parallel MT(1\bar{1}1)$. (d) Crystal structure model of magnetite with $MT(001)$, $MT(111)$ and $MT(110)$ indicated and with magnetite in the orientation of COR1A twin 2, i.e., $PL[001] \parallel MT[110]$, $PL(150) \parallel MT(\bar{1}10)$, and $PL(150) \parallel MT(1\bar{1}1)$. (e) 2D projection of the magnetite unit cell COR1A twin 1 (viewing direction $\parallel MT[\bar{1}\bar{1}0]$) and twin 2 (viewing direction $\parallel MT[110]$) according to the orientation of plagioclase in **b** with twin plane $MT(111)$, along with $MT[001]$, $MT(111)$ and $MT(110)$ indicated.

coincides with the $PL[001]$ direction, which is inclined by about 30° to the viewing direction. Thus about 30° oblique cross sections of the inclusions are observed at the sample surface. All inclusion cross sections are bounded by a combination of straight interface segments and intermittent rounded outwards convex interface segments. Typically, three pairs of parallel interface trace segments produce hexagonal cross sections. Given the acicular or prismatic shape of the magnetite inclusions, the straight interface segments are interpreted as the traces of prism planes, containing the $MT\langle 110 \rangle$ direction that is parallel to the inclusion elongation direction as the common zone axis. The three differently oriented pairs of interface traces are denoted

as F_i ($i = 1, 2, 4$). Noting that the corresponding interface planes contain both, the $MT\langle 110 \rangle$ direction that is parallel to the inclusion elongation direction and the respective interface trace on the sample surface, the three facets of the COR1A $PL[001]$ -MT inclusions are identified as $F_1 \sim \parallel PL(120)$, $F_2 \sim \parallel PL(150)$, and $F_4 \sim \parallel PL(\bar{1}50)$. This assignment is subject to some uncertainty due to the limited resolution of SEM imaging at high probe current and angular resolution of the crystal orientation determination by EBSD. Nevertheless, the fact that different inclusions show similar facet orientations suggests crystallographic control of interface orientations.

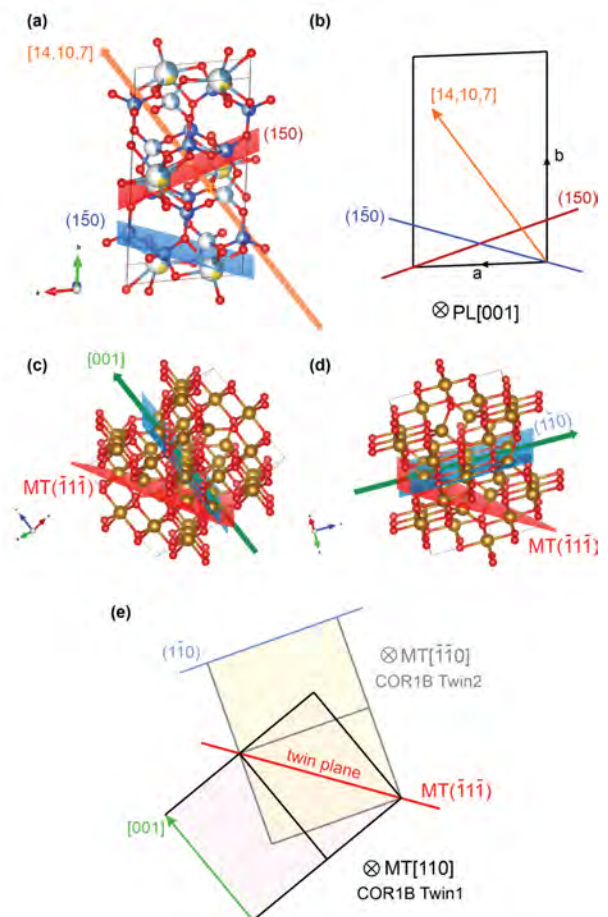


FIGURE 3. (a) Crystal structure model of plagioclase with $PL[14,10,7]$, $PL(150)$, and $PL(\bar{1}50)$ indicated. (b) 2D projection of the plagioclase unit cell viewing direction $\parallel PL[001]$ with $PL[14,10,7]$, $PL(150)$, and $PL(\bar{1}50)$ indicated. (c) Crystal structure model of magnetite with $MT[001]$, $MT(111)$, and $MT(110)$ indicated and with magnetite in the orientation of COR1B twin 1, i.e., $PL[001] \parallel MT[110]$, $PL[14,10,7] \parallel MT[001]$, and $PL(\bar{1}50) \parallel MT(1\bar{1}1)$. (d) Crystal structure of magnetite with $MT[001]$, $MT(111)$, and $MT(110)$ indicated and with magnetite in the orientation of COR1B twin 2, i.e., $PL[001] \parallel MT[110]$, $PL(150) \parallel MT(\bar{1}11)$, and $PL(150) \parallel MT(1\bar{1}0)$. (e) 2D projection of the magnetite unit cells in the orientation of COR1B twin 1 (viewing direction $\parallel MT[110]$) and twin 2 (viewing direction $\parallel MT[\bar{1}\bar{1}0]$) according to the orientation of plagioclase in **b** with twin plane $MT(111)$, along with $MT[001]$, $MT(111)$, and $MT(110)$ indicated.

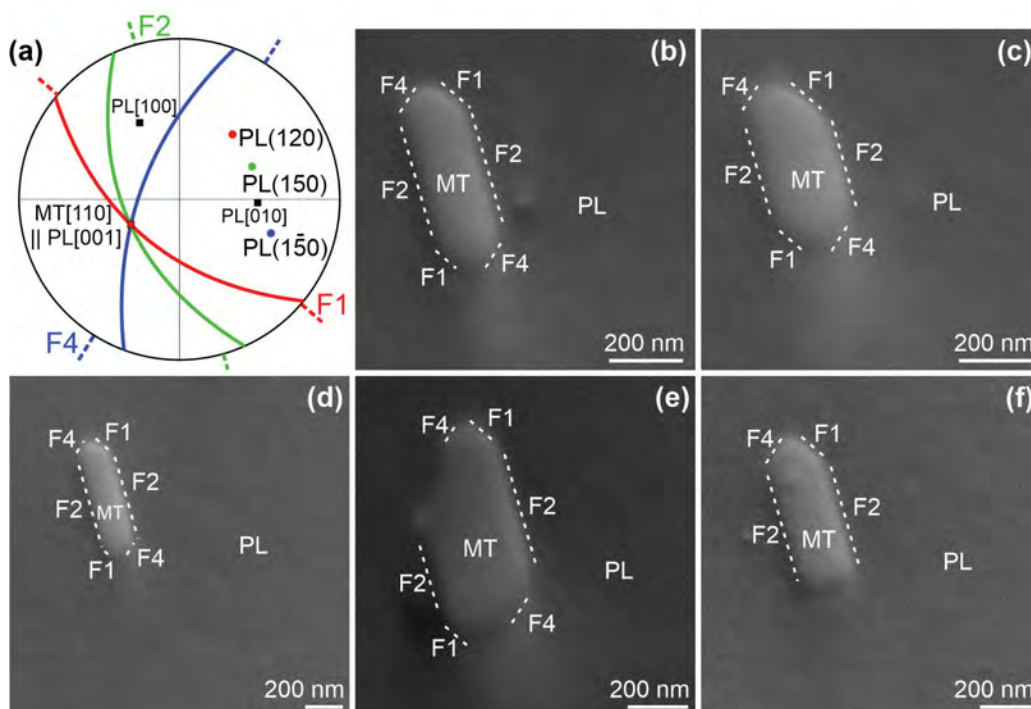


FIGURE 4. (a) Stereographic projection with viewing direction perpendicular to the specimen surface. The red, green, and blue large circles represent plagioclase lattice planes, the associated poles are labeled with the respective Miller indices. The red, green, and blue dashed straight lines indicate the traces of the facets observed in subfigures b–f. (b–f) Secondary electron images of five PL[001]-MT micro-inclusions pertaining to the COR1A variant of spinel twin 2 in plagioclase, crystallographic orientations of plagioclase and magnetite as in a. The inclusion's elongation direction is oblique to the specimen surface. The orientations of interface facet traces are highlighted with straight dashed lines and labeled as F_i ($i = 1, 2, 4$).

Microscopic interface configurations

One about 15 μm long PL[001]-MT micro-inclusion was selected for analyzing the relationships between interface orientation, crystal structure, and COR. Apart from PL[001] \parallel MT[110] the COR of the selected magnetite micro-inclusion with respect to the plagioclase host is characterized by PL(150) \parallel MT(222) and PL(150) \sim \parallel MT(220). Accordingly, the inclusion is classified as a COR1A variant pertaining to the magnetite twin 2 subgroup. A TEM foil containing a cross section of the selected inclusion was extracted using FIB technique. The foil is oriented perpendicular to the inclusion elongation direction, so that the magnetite-plagioclase interfaces are edge on. Bright-field (BF) and high-angle annular dark-field (HAADF) images of the selected inclusion cross section are shown in Figures 5a and 5b. The STEM images reveal an elongated, nearly symmetrical cross section with long and short diameters of 800 and 200 nm, respectively. Chemical analysis (see Online Materials¹ Fig. S3) confirms that the bright area in Figure 5b is due to the presence of a Ti-rich phase, which supposedly is ulvöspinel as inferred from its cubic crystal symmetry. Interestingly, Ti is enriched along the magnetite-plagioclase interface (see Online Materials¹ Fig. S3).

The inclusion cross section is bounded by four major types of interface segments labeled F_i ($i = 1, 2, 3, 4$) and three less prominent interface segments ($i = 5, 6, 7$), as indicated in Figure 5b. Atomic-scale observations at the different interface segments are shown in Figures 5c–5f and the position of each acquisition is indicated by the yellow rectangles with alphabetic

labels in Figure 5a. Interface segments F1 and F2 correspond to those shown in Figures 5d and 5f, respectively. Figure 5c relates to interface segments F5 and F6. Figure 5e shows the transition between interface segments F4 and F5. The orientations of the interface facets F_i in Figure 5b as determined from the fast Fourier transformations (FFT) of the STEM images taken at the magnetite-plagioclase interface (Online Materials¹ Fig. S4) are summarized in the second column of Table 2. Comparing the orientations of the interface facets with respect to plagioclase lattice planes obtained from STEM and SE images, the major interface segments F1, F2, and F4 in the STEM image (Fig. 5b) closely correspond to interface segments F1, F2, and F4 in the SE images (Fig. 4).

High-resolution iDPC-STEM images of the magnetite-plagioclase interface acquired at different interface segments are shown in Figures 5c–5f. Note that the iDPC-STEM images shown in Figures 5c–5f are somewhat rotated with respect to one another as can be seen from the traces of equivalent lattice planes in the different images. It can be seen in the iDPC-STEM images that the magnetite inclusion is in direct contact with the plagioclase host at each interface segment, and neither gaps nor amorphous layers are observed anywhere along the interface. The strong contrast at the interface is an artifact related to the “delocalization” effect, which is due to the large convergence angle of 30 mrad, which was chosen to achieve the highest possible spatial resolution. In this case, the electron rays of the beam are not perfectly parallel to the magnetite-plagioclase interface,

TABLE 2. Faceted interface Fi ($i = 1-7$) configurations of a PL[001]-MT COR1A micro-inclusion

Fi	Orientation	Δg_i	Definition	Δg^f
				Orientation
F1	MT(0.296, -0.296, 0.908) \sim PL(470)	$g_{MT}(\bar{1}\bar{1}\bar{1}) - g_{PL}(\bar{1}20)$		MT f (0.193, -0.193, 0.962)
F2	MT(-0.543, 0.543, -0.641) PL(140)	$g_{MT}(00\bar{1}) - g_{PL}(\bar{1}\bar{1}0)$		MT f (-0.577, 0.577, -0.577)
F3	MT(-0.611, 0.611, -0.503) PL(180)	$g_{MT}(\bar{1}\bar{1}\bar{3}) - g_{PL}(220)$		MT f (-0.577, 0.577, -0.577)
F4	MT(0.698, -0.698, 0.158) PL(170)	$g_{MT}(\bar{1}\bar{1}2) - g_{PL}(2\bar{1}0)$		MT f (0.688, -0.688, -0.230)
F5	MT(0.509, -0.509, -0.694) PL(670)	$g_{MT}(\bar{1}\bar{1}\bar{1}) - g_{PL}(030)$		MT f (0.503, -0.503, -0.703)
F6	MT(-0.076, 0.076, -0.994) PL(210)	$g_{MT}(220) - g_{PL}(\bar{1}40)$		MT f (-0.192, 0.192, -0.962)
F7	MT(0.689, -0.689, -0.226) PL(130)	$g_{MT}(\bar{1}\bar{1}0) - g_{PL}(0\bar{1}0)$		MT f (0.688, -0.688, -0.229)

Notes: The first column represents each of the different interface segments as indicated in Figure 5b. The second column represents each facet's orientation with respect to magnetite (by Δg calculation) and plagioclase (by FFT estimation) lattice planes. The third column gives the definition of each facet related Δg defined by the g vectors of magnetite and plagioclase. The last column represents the orientation of each constrained MT f -PL interface facet with respect to the lattice plane of the constrained magnetite unit cell (by Δg^f calculation).

which causes the pronounced contrasts along the phase boundaries (Borisevich et al. 2006).

Different orientation relationships between lattice fringes of the two phases and the interface trace are observed along the different interface segments. In Figure 5c three interface segments are seen. The uppermost segment is parallel to the MT($\bar{1}\bar{1}\bar{1}$) lattice fringes, and it is approximately parallel to PL($\bar{2}30$), but no lattice fringes corresponding to this lattice plane are visible in plagioclase. The second segment is parallel to the PL($\bar{1}10$) lattice fringes, and it is approximately parallel to MT($2\bar{2}\bar{3}$), but no lattice fringes corresponding to this lattice plane are visible in magnetite. The lowermost interface segment is approximately parallel to PL(210), but neither the MT(001) nor the PL(110) planes, the lattice fringes of which are visible, are parallel to this interface segment. In Figure 5d, the interface is perfectly straight on the tens of nanometer scale but neither the lattice fringes discernible in plagioclase nor those discernible in magnetite are parallel to the interface plane. The interfaces in Figures 5e and 5f are curved on the 10s of nm scale and are stepped on the atomic scale. In Figure 5e the terraces, the long sides of the steps, are parallel to the PL($\bar{1}30$) lattice fringes, but no lattice fringes parallel to the terraces are visible in magnetite. By contrast, in Figure 5f the terraces are parallel to the MT($\bar{1}\bar{1}\bar{1}$) lattice fringes, but no lattice fringes parallel to the terraces are visible in plagioclase.

Interface configuration of a COR1B PL[001]-MT inclusion

High-resolution iDPC-STEM images of different magnetite-plagioclase interface segments of a PL[001]-MT inclusion pertaining to the COR1B orientation variant are shown in Figure 6. The COR of this magnetite inclusion to the plagioclase host is obtained from FFT analyses of an iDPC-STEM image (Online Materials¹ Fig. S5). The specimen was prepared without prior optical documentation and EBSD analysis and so the morphology of the inclusion and its SOR with respect to the plagioclase host are not known. Based on the fact that the inclusion pertains to the COR1B variant, it may be supposed that it is a needle-shaped inclusion. The viewing direction is parallel to PL[001] in all subfigures. In this projection prominent channels running parallel to PL[001] in the crystal structure of plagioclase are edge on and appear as six-membered rings of SiO₄ and AlO₄ tetrahedra (see crystal structure models in Figs. 6d and 6e). Small deviations between the MT[110] direction and the PL[001] direction can be discerned when plagioclase is in the PL[001] zone axis during the acquisition, and magnetite is slightly off the MT[110] zone axis. Nevertheless, continuous layers with intermediate gray contrast parallel to MT(001) alternating with arrays of isolated spots with

relatively bright contrast can be discerned in magnetite. The continuous layers correspond to layers comprised of alternating tetrahedrally and octahedrally coordinated Fe-atoms parallel to

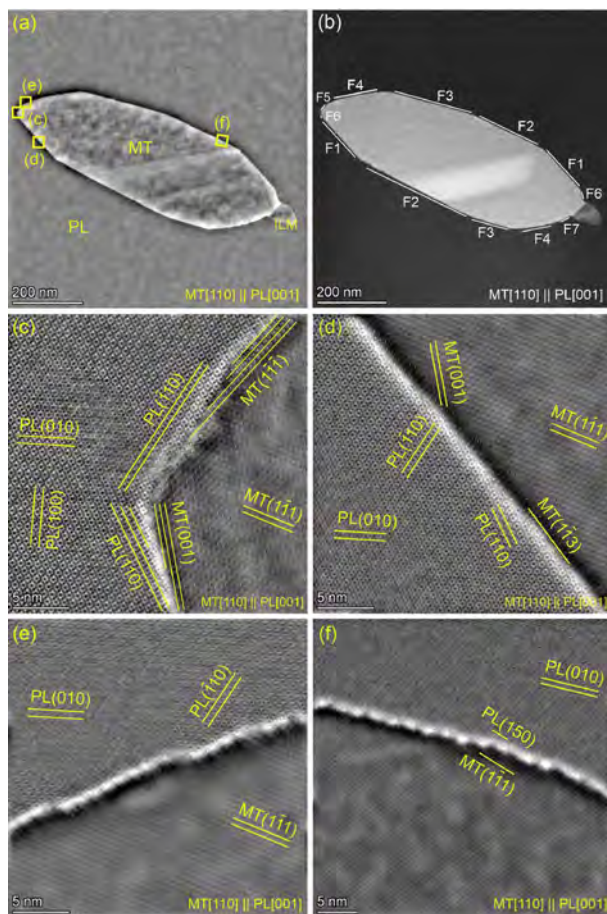


FIGURE 5. (a) Bright-field image showing the cross section of a selected COR1A PL[001]-MT inclusion. The viewing direction is parallel to MT[110] || PL[001] in all subfigures. The positions, where the iDPC-STEM images shown in c-f were taken, are marked by yellow squares with corresponding alphabetical labels. (b) High-angle annular dark-field (HAADF) image of the inclusion shown in a. The bright domain within magnetite is ulvöspinel. The different facets of the magnetite-plagioclase interface are labeled as Fi ($i = 1-7$); (c-f) iDPC-STEM images of different magnetite-plagioclase interface segments. Characteristic lattice planes in magnetite and plagioclase are indicated. Slight rotations around the viewing direction exist among acquisitions, for reference some lattice plane traces are indicated.

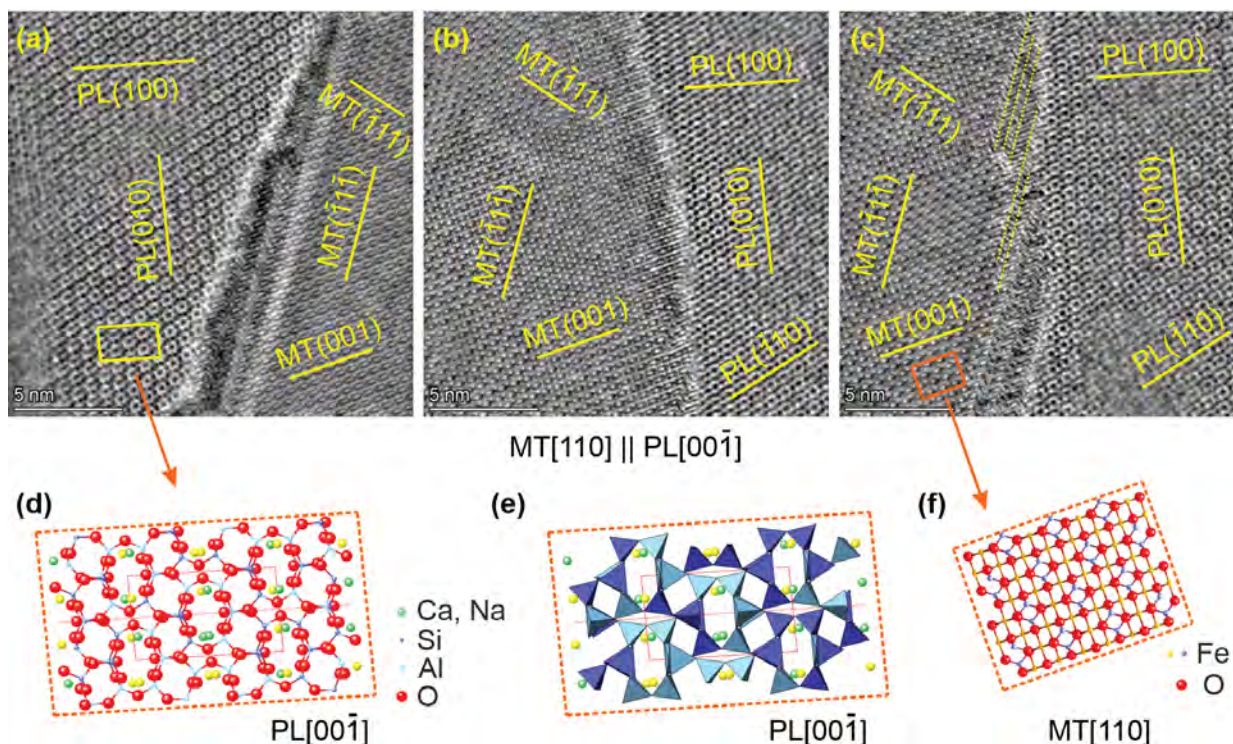


FIGURE 6. High-resolution iDPC-STEM images of different magnetite-plagioclase interface segments of a COR1B PL[001] inclusion. The viewing direction is parallel to PL[001] in all subfigures, as MT[110] and PL[001] are not perfectly parallel in COR1B PL[001] inclusions, magnetite is slightly off the MT[110] zone axis. Some low-index lattice planes are indicated for both magnetite and plagioclase. Within the plagioclase domain, channels parallel to PL[001] appear as six-membered rings. Crystal structure models of plagioclase and magnetite in appropriate orientations are shown for reference. Purple and yellow spheres in the stick and ball crystal structure models of magnetite represent tetrahedrally and octahedrally coordinated Fe cations, respectively. (a) Plagioclase (left) and magnetite (right) with stacking faults parallel to MT($\bar{1}\bar{1}\bar{1}$) in magnetite close to the magnetite-plagioclase interface. (b) Magnetite (left) and plagioclase (right) with continuous layers parallel MT(001) apparently kinked in the immediate vicinity of the magnetite-plagioclase interface so that they meet up with the six membered rings representing the channels parallel to PL[001] in plagioclase. (c) Magnetite (left) and plagioclase (right) with domains along the magnetite-plagioclase interface, where the columns of octahedrally coordinated Fe atoms parallel MT(001) are missing—possibly constituting a new phase. (d) Ball-stick model of plagioclase crystal structure according to the yellow box in a. (e) Polyhedral model of plagioclase crystal structure according to d. (f) Ball-stick model of magnetite crystal structure according to the orange box in c.

MT(001), the isolated spots with bright contrast correspond to columns of octahedrally coordinated Fe-atoms extending parallel to MT[110] (Fig. 6).

The different segments of the magnetite-plagioclase interfaces shown in Figures 6a–6c are all wavy in appearance. In the high-resolution iDPC-STEM image of Figure 6b it can be seen that at the magnetite-plagioclase interface the continuous layers parallel to MT(001) are connected to the six-membered rings representing the channels parallel to PL[001] in the plagioclase crystal structure. Apparently along the magnetite-plagioclase interface the spacing between the channels parallel PL[001] in plagioclase and the spacing between two continuous layers parallel to MT(001) in magnetite along the magnetite-plagioclase interface is different, and the MT(001) layers link up with the six-membered rings at different positions within the rings. In some places, the MT(001) layers are kinked in the immediate vicinity to the magnetite-plagioclase interface, so that they link up with the six membered rings (see bottom of Fig. 6b). In addition, at some interface segments, magnetite appears to undergo a structural transformation close to the magnetite-plagioclase

interface. For example, at the interface segment shown in the upper part of Figure 6c the bright spots representing the arrays of individual columns of octahedrally coordinated Fe atoms disappear in an about 1 nm wide zone along the interface, while the structure of the new phase clearly inherits elements from the previous magnetite structure.

Finally, two-dimensional defects seem to have been introduced close to the magnetite-plagioclase interface, through which parts of the magnetite grain that are in direct contact with the plagioclase are displaced with respect to the remainder of the magnetite grain (Fig. 6a). A particularly instructive example is shown in Figure 7, where stacking faults are present in the magnetite in the area highlighted by the green rectangle. A closeup of the domain is shown in Figure 7b. Two stacking faults can be discerned. One is parallel to MT($\bar{1}\bar{1}\bar{1}$) and the second is parallel to MT($\bar{1}\bar{1}\bar{1}$) (see Fig. 7c). The two stacking faults correspond to Shockley partial dislocations. The stacking fault parallel to MT($\bar{1}\bar{1}\bar{1}$) has a displacement vector $\mathbf{b} = 1/6[1\bar{1}\bar{2}]$ and the stacking fault parallel to MT($\bar{1}\bar{1}\bar{1}$) has a displacement vector $\mathbf{b} = 1/6[\bar{1}\bar{1}\bar{2}]$. The magnetite domain bounded by the two stacking faults is thus shifted with respect to the bulk magnetite

grain by $1/6[1\bar{1}\bar{2}] + 1/6[\bar{1}\bar{1}\bar{2}] = 2/3[00\bar{1}]$. A schematic sketch of this situation is shown in Figure 7c. The black circles represent the O atoms in the original magnetite crystal. The two small red arrows emanating from one O atom indicate the $1/6[1\bar{1}\bar{2}]$ and $1/6[\bar{1}\bar{1}\bar{2}]$ displacements associated with the two stacking faults. Cooperative application of these two displacements results in an overall $2/3[00\bar{1}]$ displacement, which is indicated by the heavy red arrow. Application of the overall displacement to the oxygen sub-lattice of the original magnetite grain produces the oxygen sub-lattice of the displaced magnetite domain, which is shown in blue.

DISCUSSION

Genesis of PL[001]-MT inclusions

Based on the notion that the plane-normal type magnetite micro-inclusions occur in pristine plagioclase domains typically in the core regions of the grains, whereas the PL[001]-MT inclusions typically occur at the transition between pristine and hydrothermally altered domains, it is inferred that the PL[001]-MT inclusions formed later than the plane-normal type magnetite micro-inclusions. Indeed, petrographic evidence (Fig. 1) suggests that the PL[001]-MT inclusions formed by recrystallization from the pre-existing plane-normal type magnetite micro-inclusions. The spatial association with healed cracks and with the external portions of the plagioclase grains suggests that this recrystallization took place during hydrothermal overprint. Detailed descriptions of the hydrothermal history of the gabbroic rocks from comparable samples from the same dredge location can be found in Pertsev et al. (2015). The plane normal inclusions were inferred to have precipitated from Fe-bearing magmatic plagioclase during a late magmatic stage at temperatures in excess of about 600 °C (Bian et al. 2021). The PL[001] type inclusions formed at a later stage, probably at lower temperatures. This inference is corroborated by the fact that PL[001]-MT micro-inclusions typically contain precipitates of ulvospinel, which form by exsolution from Ti-bearing magnetite at temperatures ≤ 600 °C (Tan et al. 2016). In contrast, the magnetite micro-inclusions of the plane normal type contain lamellar precipitates of ilmenite that are supposedly formed by high-

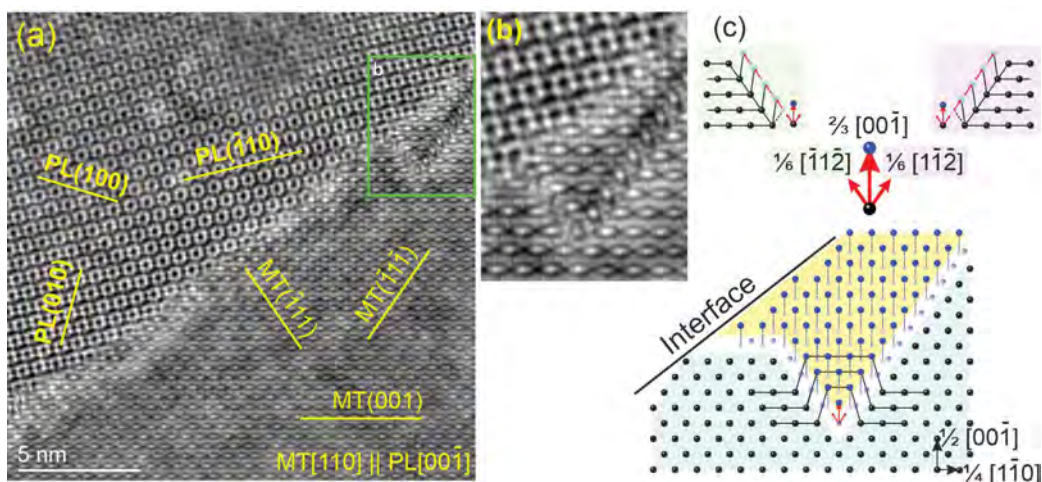
temperature oxidation at ≥ 600 °C (Bian et al. 2021). Furthermore, in some places, the secondary nature of the PL[001]-MT micro-inclusions is evident from PL[001]-MT inclusions growing on pre-existing plane-normal magnetite inclusions (Fig. 1c).

Crystallographic basis for the SOR and CORs of PL[001]-MT inclusions

Out of the three COR variants of the PL[001]-MT micro-inclusions listed in Table 1 COR1A and COR1B are related by a 70° rotation about PL[001] \parallel MT[110]. In variant COR2, the PL[001] and MT[110] directions are slightly misaligned, and bringing COR2 magnetite into COR1B orientation could be envisaged as a $\sim 5^\circ$ rotation of the COR2 magnetite about MT($\bar{1}\bar{1}\bar{1}$) \parallel PL(120) that makes MT[110] parallel to PL[001] followed by a $\sim 120^\circ$ rotation about MT[110] \parallel PL[001], which makes the close-packed oxygen layers parallel to MT($\bar{1}\bar{1}\bar{1}$) in magnetite parallel to the oxygen layers parallel to PL(150) in plagioclase, which corresponds to COR1B. A similar combination of rotations can be applied for relating the COR2 and COR1A variants.

Each COR variant has two subgroups that are related by the spinel twin law. As shown in Table 1 and Figures 2–3, in magnetite twin 1, we have PL[-14,10,-7] \parallel MT[001] for COR1A and PL[14,10,7] $\sim \parallel$ MT[001] for COR1B. These CORs have been classified as PL[001] type magnetite micro-inclusions in “nucleation orientation” by Ageeva et al. (2020). The plagioclase crystal structure contains channels parallel to PL[001], which appear as six-membered rings of SiO₄ and AlO₄ tetrahedra in a projection parallel to PL[001] (see Fig. 6). The nucleation orientation is defined by the alignment of FeO₆ octahedra, which are basic building units of the magnetite crystal structure so that they fit into these channels. The distance between two opposite apices of a FeO₆ octahedron is about 4.28 Å, and the line connecting opposing apices corresponds to one of the MT<100> directions. There are several orientations in which the FeO₆ octahedra fit into the channels, including orientations where MT<100> is parallel to PL[14,10,7], PL[-14,10,-7], PL[023], or PL[0 $\bar{2}\bar{3}$]. We suppose that the good fit of FeO₆ octahedra in the channels of the plagioclase crystal structure ensures a low-energy barrier

FIGURE 7. (a) Magnetite-plagioclase interface of the same COR1B type magnetite micro-inclusion as shown in Figure 6 with stacking faults in magnetite highlighted with the green rectangle. (b) Closeup of the interface segment with associated stacking faults in the upper part of a. The images have been rotated relative to Figure 6 so that the MT(001) lattice planes are horizontal. (c) Sketch of the arrangement of O atoms in the magnetite crystal structure as observed in b.



for magnetite nucleation, and thus the channels are preferred sites for nucleation of magnetite in plagioclase (Wenk et al. 2011; Ageeva et al. 2020).

If magnetite is present as magnetite twin 2, the COR1A and COR1B variants correspond to the PL[001] type magnetite micro-inclusions in “main orientation” (Ageeva et al. 2020), which ensures parallel alignment of important oxygen layers in plagioclase and in magnetite. “Important oxygen layers in plagioclase” we define as concentrations of O atoms forming roughly planar, several atomic layers thick configurations parallel to certain plagioclase lattice planes. In magnetite, we consider the close-packed oxygen layers, such as MT(222) lattice plane, as “important oxygen layers in magnetite.” In several places, the facets of the magnetite-plagioclase interface are parallel to important oxygen layers in the magnetite and plagioclase crystal structures. For instance, in examples of COR1A magnetite twin 2 the magnetite-plagioclase interface follows PL(150) || MT(110) as shown in Figure 2, and in examples of COR1B magnetite twin 2 the interface follows PL(150) || MT(110), as shown in Figure 3. These interface facets contain the elongation direction of the inclusions and thus form prismatic facets. The parallel alignment of oxygen layers in magnetite and plagioclase probably represents a low-energy configuration. In addition, it minimizes the distances over which O atoms need to be shifted during the replacement of plagioclase by magnetite and thus lowers the energy barrier for magnetite growth within plagioclase host (Hwang et al. 2019).

In summary, all six COR variants of the PL[001] type magnetite micro-inclusions are related by crystallographic operations, which strongly suggests that the CORs of the PL[001] type magnetite inclusions to the plagioclase host are controlled by crystal structure fit between the two phases. In particular, the fit of the oxygen sub-lattices appears to be optimized across the magnetite-plagioclase interfaces. On the one hand, the good fit of the oxygen sub-lattices ensures low-energy configurations and thus influences the CORs between the magnetite micro-inclusions and the plagioclase host. On the other hand, certain orientation variants, the two nucleation orientations, minimize the nucleation barrier and others minimize the extent over which oxygen ions must be displaced during the replacement of plagioclase by magnetite. The latter two phenomena ease magnetite nucleation and growth and thus influence the kinetics of magnetite precipitation in plagioclase host.

Crystallographic control on interface orientations of COR1A PL[001]-MT inclusions

Interface segments following certain directions that are similar for different magnetite inclusions in a single-plagioclase domain and curved interface segments comprised of steps following lattice fringes in either plagioclase or magnetite indicate that interface orientations are crystallographically controlled. In microstructural equilibrium, interface orientations are selected so that the system attains a low-energy configuration. Ultimately, interfacial energy in crystalline materials depends on the microscopic structure of the interface (Sutton and Balluffi 1995; Zhang 2020). In detail, quantification of interfacial energy is difficult and is beyond the scope of this work. We follow an alternative approach based on the notion that the degree

of geometrical match between the lattices of magnetite and plagioclase along their interfaces provides a qualitative indication of interfacial energy. In the following, HR STEM images and corresponding simulated diffraction patterns are analyzed to shed light on the relationships between magnetite-plagioclase interface orientations and the degree of lattice match between the two phases.

In Figure 8, simulated diffraction patterns of magnetite (red spots) and plagioclase (black spots) are superimposed according to the orientation relationship obtained from the STEM images shown in Figure 5. The viewing direction is parallel to MT[110] || PL[001]. The diffraction spots define the reciprocal lattice vectors $\mathbf{g}_\kappa(hkl)$, where κ indicates the phase, plagioclase or magnetite, and (hkl) are the Miller indices of the lattice plane represented by the respective \mathbf{g} vector. The difference vector between a magnetite and a plagioclase reciprocal lattice vector is denoted as $\Delta\mathbf{g} = \mathbf{g}_{\text{MT}} - \mathbf{g}_{\text{PL}}$ (Hirsch 1977). It can be shown that the lattice planes represented by $\mathbf{g}_{\text{MT}}(hkl)$ and $\mathbf{g}_{\text{PL}}(hkl)$ meet in a coherent fashion at a plane that is oriented perpendicular to the corresponding $\Delta\mathbf{g}$ vector (Bäro and Gleiter 1974; Luo and Weatherly 1988). Such a plane is supposed to have lower interfacial energy as compared to other interface orientations. This would make such an interface prone to forming a facet of the magnetite-plagioclase interface (Zhang and Purdy 1993; Zhang and Weatherly 2005). The arrows in Figure 8 mark two pairs of nearly coinciding diffraction spots $\mathbf{g}_{\text{MTI}} = \text{MT}(\bar{1}13)$,

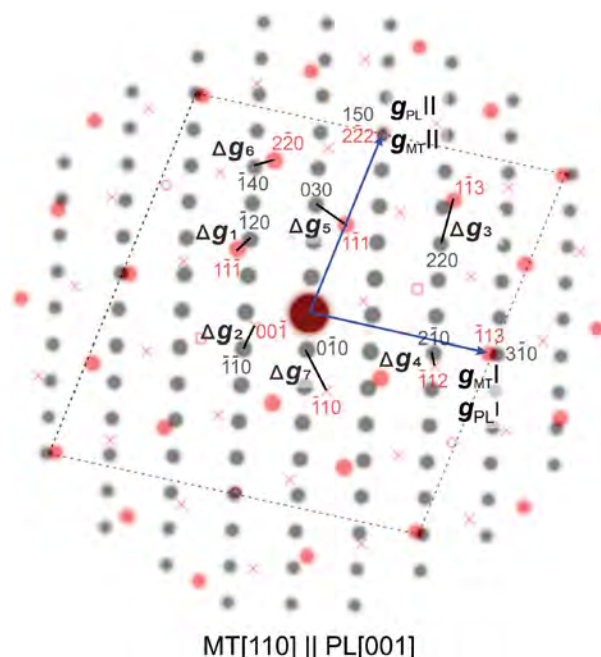


FIGURE 8. Simulated diffraction patterns of magnetite (red spots) and plagioclase (black spots) superimposed according to the orientation relationship obtained from the fast Fourier transformation (FFT) upon STEM images in Figure 5d under viewing direction MT[110] || PL[001]. Near coincident diffraction spots \mathbf{g}_{PLI} , \mathbf{g}_{MTI} and \mathbf{g}_{PLII} , \mathbf{g}_{MTII} are indicated with arrows. $\Delta\mathbf{g}$, connecting diffraction spots of magnetite and plagioclase that are perpendicular to the corresponding facets F_i in Figure 5b are indicated therein. The related diffraction spots of magnetite are indexed in red and of plagioclase are indexed in black.

TABLE 3. Lattice constants of plagioclase (PL) taken from Wenk et al. (1980) and of magnetite (MT) taken from Fleet (1981)

Phase	<i>a</i> /Å	<i>b</i> /Å	<i>c</i> /Å	α°	β°	γ°
PL	8.1736	12.8736	7.1022	93.462	116.054	90.475
MT	8.3970	8.3970	8.3970	90	90	90
MT ^c	8.3145	8.3156	8.0757	91.0735	88.9688	89.2397

Note: In the last row the lattice constants of constrained magnetite, MT^c are given.

$\mathbf{g}_{\text{PLI}} = \text{PL}(3\bar{1}0)$, and $\mathbf{g}_{\text{MTII}} = \text{MT}(2\bar{2}2)$, $\mathbf{g}_{\text{PLII}} = \text{PL}(150)$. Together with their symmetrical equivalents they bound a parallelogram within the diffraction patterns shown in Figure 8 containing the diffraction spots of low-index lattice planes from magnetite and plagioclase. Within this parallelogram seven $\Delta\mathbf{g}_i$ ($i = 1-7$) vectors can be identified that are perpendicular to the traces of the magnetite-plagioclase interfaces shown in Figure 5b. The definitions of these $\Delta\mathbf{g}_i$ ($i = 1-7$) vectors are listed in the third column of Table 2. The orientations of interface segments F_i ($i = 1-7$) can thus be determined from the related $\Delta\mathbf{g}_i$ vectors. The interface orientations expressed in terms of Miller indices referring to magnetite and to plagioclase are listed in the second column of Table 2.

Growth of magnetite within plagioclase implies motion of magnetite-plagioclase interfaces into the plagioclase. Across these interfaces, the triclinic lattice of plagioclase is transformed into the cubic lattice of magnetite. In the following, we apply a constraint to one of the crystal lattices so that a more direct geometrical relationship between the two lattices is produced. We then check whether in the constrained configuration, geometrical models for describing the crystallographic relationships at the interface may be applied to explain interface orientations. For defining the transformation from the lattice of plagioclase to the lattice of magnetite, the metrics of the two lattices and their COR must be known. The lattice parameters of plagioclase and magnetite are taken from Wenk et al. (1980) and Fleet (1981), respectively, as listed in the first two rows of Table 3. The COR between plagioclase and magnetite of the inclusion under study is known from EBSD and HR STEM data. For obtaining the transformation matrix relating the two lattices three non-planar vectors are selected as a base within each of the lattices. One base vector is selected along the inclusion elongation direction, where $\text{MT}[330] \parallel \text{PL}[005]$ as $3 \times \text{MT}[110]$, $3 \times d_{\text{MT}[110]} = 3 \times 11.871 \text{ \AA} = 35.613 \text{ \AA}$ is nearly identical in length to $5 \times \text{PL}[001]$, $5 \times d_{\text{PL}[001]} = 5 \times 7.1022 \text{ \AA} = 35.511 \text{ \AA}$. The other two base vectors are obtained by comparing the diffraction patterns of the two phases in Figure 8. In the superimposed diffraction patterns, two pairs of nearly identical \mathbf{g}_k vectors are identified. The two pairs are formed by $\mathbf{g}_{\text{PLI}} = \text{PL}(3\bar{1}0)$ together with $\mathbf{g}_{\text{MTI}} = \text{MT}(\bar{1}13)$, and by $\mathbf{g}_{\text{PLII}} = \text{PL}(150)$ together with $\mathbf{g}_{\text{MTII}} = \text{PL}(2\bar{2}2)$ (see Fig. 8). These \mathbf{g}_k vectors are selected as the second and third base vectors for the plagioclase and magnetite lattices. Perfect coincidence of the selected \mathbf{g}_{PLI} and \mathbf{g}_{MTI} and of the \mathbf{g}_{PLII} and \mathbf{g}_{MTII} vectors can be obtained by applying a small strain to either one or to both lattices. Assuming the necessary strain is within the elastic limit, the exact strain could be calculated for both lattices, if the elastic constants are known. We take an alternative approach and test the two extreme scenarios, where only one lattice is strained while the other remains unstrained. The procedure for calculating the lattice of constrained magnetite to make it fit to the lattice of unstrained plagioclase is described in the Online Materials¹ 2

(Shi et al. 2013, 2021).

The lattice parameters of constrained magnetite, MT^c, are given in Table 3. It is seen that the lattice parameters of MT^c only slightly differ from those of unconstrained magnetite. Figure 9a shows the simulated diffraction patterns of plagioclase and constrained magnetite MT^c superimposed on one another according to the observed COR over a large diffraction area. The red and black spots represent the diffraction pattern of constrained magnetite and plagioclase, respectively. Figures 9b–9c show the simulated diffraction patterns of constrained magnetite MT^c and plagioclase according to the COR over the central parallelogram area, respectively. Figure 9d shows the superimposed diffraction patterns of Figures 9b–9c over a smaller diffraction area with the same color codes for constrained magnetite and plagioclase as in Figure 9a. Through the application of the constraint, several diffraction spots have become coincident, and they are marked with circles. Moreover, several of the $\Delta\mathbf{g}$ vectors have become parallel. We refer to the \mathbf{g} vectors of constrained magnetite as \mathbf{g}_{MT}^c vectors and to the $\Delta\mathbf{g}$ vectors defined by the difference between \mathbf{g}_{MT}^c and \mathbf{g}_{PL} as $\Delta\mathbf{g}^c$. The orientations of $\Delta\mathbf{g}_i^c$ values with respect to the MT^c crystal coordinate system are given in the last column of Table 2. Within the quadrilateral domain defined by the coinciding diffraction spots (dashed line in Fig. 9d), three pairs of $\Delta\mathbf{g}_i^c$ vectors, which have been non-parallel before the application of the constraint, have become perfectly parallel $\Delta\mathbf{g}_i^c$ vectors in the constrained configuration: $\Delta\mathbf{g}_1^c \parallel \Delta\mathbf{g}_6^c$, $\Delta\mathbf{g}_2^c \parallel \Delta\mathbf{g}_5^c$, and $\Delta\mathbf{g}_4^c \parallel \Delta\mathbf{g}_7^c$. While the superimposed magnetite and plagioclase diffraction patterns in the unconstrained configuration (Fig. 8) yield seven $\Delta\mathbf{g}_i$ vectors defined by low-index lattice planes of magnetite and plagioclase, each corresponding to a specific magnetite-plagioclase interface orientation, only four $\Delta\mathbf{g}_i^c$ values remain after application of the constraint, indicating that only four interface orientations would be preferred in the constrained configuration. For three out of the four preferred interface orientations remaining in the constrained configuration, two perfectly identical $\Delta\mathbf{g}_i^c$ vectors exist, each one defined by two different pairs of lattice planes in magnetite and plagioclase. This implies that each of these interface planes corresponds to an “exact interface” in the sense of Robinson et al. (1971), across which all lattice planes containing the viewing direction as the common zone axis are coherent. This configuration ensures a perfect match between the magnetite and plagioclase lattice planes sharing this common zone axis, and these lattice planes are continuous across the interface (Hwang et al. 2010; Zhang and Yang 2011).

Some of the lattice points of constrained magnetite and of plagioclase coincide constituting the constrained coincidence site lattice (CCSL). Figures 9e–9f represent the correspondence of the lattice points of constrained magnetite and plagioclase in real space. Both figures are oriented according to Figure 9a. The viewing direction is parallel to the inclusion elongation direction $\text{PL}[001] \parallel \text{MT}^c[110]$. For reference, a Cartesian coordinate system is introduced where the horizontal direction is taken as the *X*-axis, which corresponds to the $[-0.162, 0.162, 0.973]$ direction of constrained magnetite and to the $[0.891, 0.033, 0.453]$ direction of plagioclase. The vertical axis is taken as the *Y*-axis, which corresponds to the $[0.69, -0.69, 0.216]$ direction of constrained magnetite and to the $[0.045, 0.995, 0.086]$ direction of plagioclase. In Figure 9e, the CCSL points in different layers within

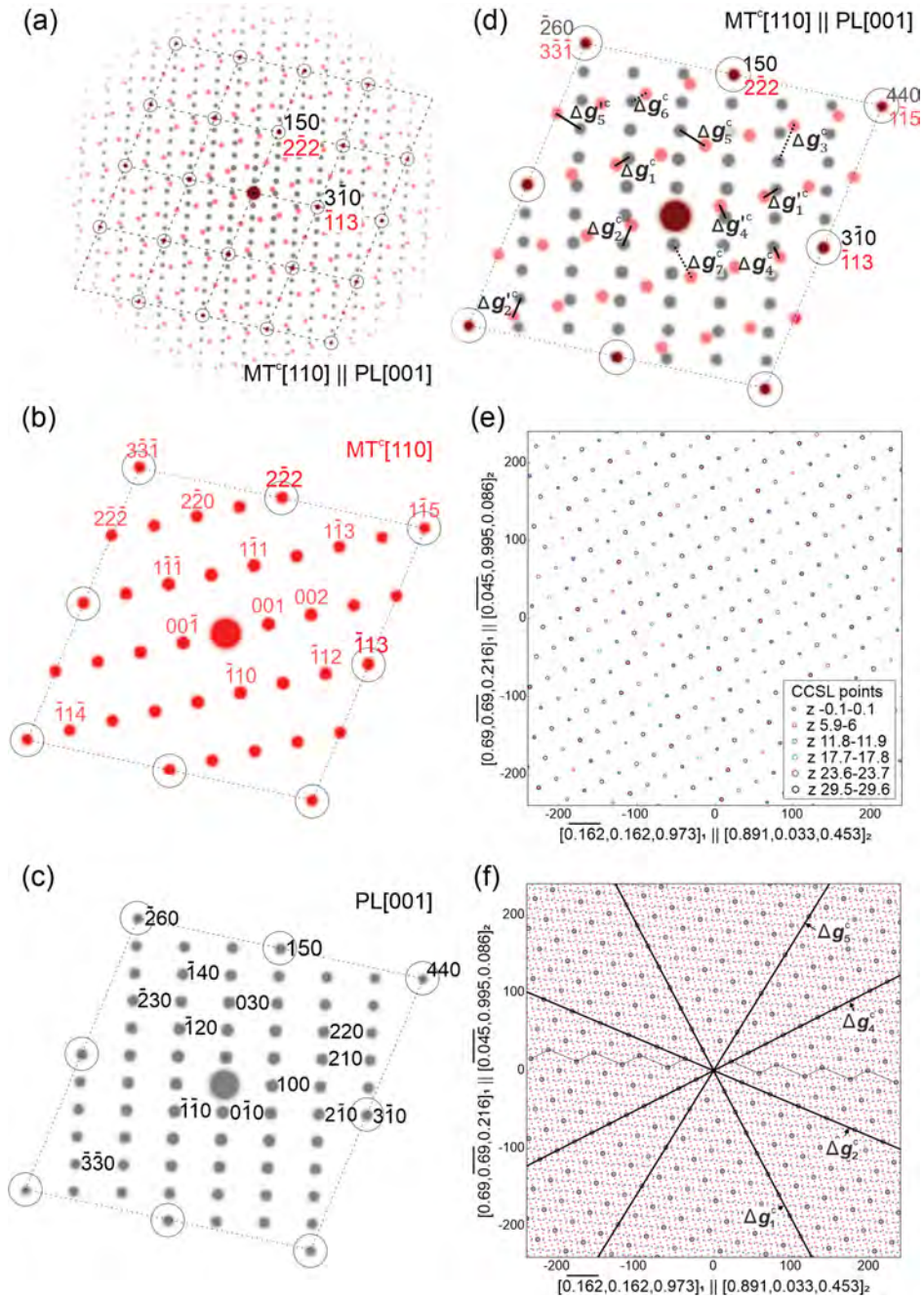


FIGURE 9. (a) Simulated diffraction patterns of constrained magnetite MT^c (red) and plagioclase (black) superimposed according to the observed orientation relationship. The coincident diffraction spots are referred to as CCSL points, which are highlighted with black circles, and the black dashed lines represent the CCSL in reciprocal space. (b) Simulated diffraction patterns of constrained magnetite according to the orientation in a over the central area with the Miller indices of the diffraction spots related to the Δg_i^c values indicated. (c) Simulated diffraction spots of plagioclase according to the orientation in a over the central area with the Miller indices of the diffraction spots related to the Δg_i^c indicated. (d) Closeup of the central CCSL marked in a. Among the constrained Δg_i^c values, Δg_5^c , Δg_6^c , and Δg_7^c have become parallel to Δg_5^c , Δg_4^c , and Δg_3^c (dashed lines). Δg_i^c values associated with different Δg_{MT}^c and g_{PL} that are found to be parallel to the aforementioned Δg_i^c values are indicated. (e–f) CCSL points plotted in real space with orientations according to a; the Z axis is parallel to the viewing direction. Axes labels indicate lattice directions of constrained magnetite (denoted as 1) and plagioclase (denoted as 2), the units on the axes are in angstroms. (e) CCSL points in real space at different positions along the Z axis in the range of $Z = [-0.1, 29.6]$ Å, the different colors correspond to Z coordinate (see legend). (f) Relationships between interface facets' orientations and corresponding Δg_i^c values, and the facets' intersections with the CCSL (black circles) within one repetition unit. Red and blue spots represent lattice points of constrained magnetite and plagioclase, respectively. Dashed lines represent a preferred terrace and ledge configuration observed at interface F2.

the range of $Z = [-0.1, 29.6] \text{ \AA}$ are indicated, where the different colors correspond to different positions along the Z axis (see legend). For clarity, the lattice points of constrained magnetite and plagioclase have been omitted. This pattern repeats along the Z direction after a distance of $MT[330] = PL[005]$. The facet orientations corresponding to the different Δg_i^f values are shown in Figure 9f. The red and blue spots in Figure 9f represent lattice points of constrained magnetite and of plagioclase, respectively, in real space. The CCSL points are marked with black circles. Each facet is parallel to linear arrays of CCSL points, and the facet orientations are consistent with the observed facets of the selected $PL[001]$ - MT micro-inclusion. The facet perpendicular to Δg_4^f has the highest density of CCSL points followed by the facet perpendicular to Δg_1^f and the facet perpendicular to Δg_5^f . Finally, Δg_3^f has the lowest density of CCSL points in the 2D projection. Since the CCSL points in the range of $Z = [-0.1, 29.6] \text{ \AA}$ are distributed over different positions along the inclusion elongation direction, it is essential to also examine the CCSL points within each facet. The CCSL points in the different interface planes are shown in Figure 10. In each plot, the viewing direction is parallel to the corresponding Δg_i^f vector, the horizontal direction is the inclusion elongation direction, and the vertical direction is the in-plane direction in the respective interface facet that is per-

pendicular to the inclusion elongation direction. The two dashed vertical lines in each plot indicate the range of $Z = [-0.1, 29.6] \text{ \AA}$. Red and blue spots are lattice points of constrained magnetite and of plagioclase, respectively. CCSL points are highlighted with circles. The absolute number of CCSL points within the range of $Z = [-0.1, 29.6] \text{ \AA}$ in each facet plane is indicated above each plot. From this number the areal density of CCSL points can be calculated for each facet plane. The relative proportions are similar to the density of the CCSL points on the interface traces in the 2D projection. The facet perpendicular to Δg_4^f has the highest areal density of CCSL points, followed by the facet perpendicular to Δg_1^f and the facet perpendicular to Δg_5^f . The facet perpendicular to Δg_3^f has the lowest areal density of CCSL points.

Our observations corroborate the supposition that a high area density of CCSL points in the interface plane serves as a criterion for the selection of specific interface facets (Ye and Zhang 2002). For example, for the commonly observed interface facet F1, which typically is sharp and straight on the atomic scale (Fig. 5d), the area density of CCSL points corresponding to Δg_1^f (Fig. 9d) is relatively high. The F1 interface segment is thus supposed to represent a low-energy configuration. In contrast, for the least commonly observed interface segment F5, the area density of CCSL points is indeed substantially lower than for

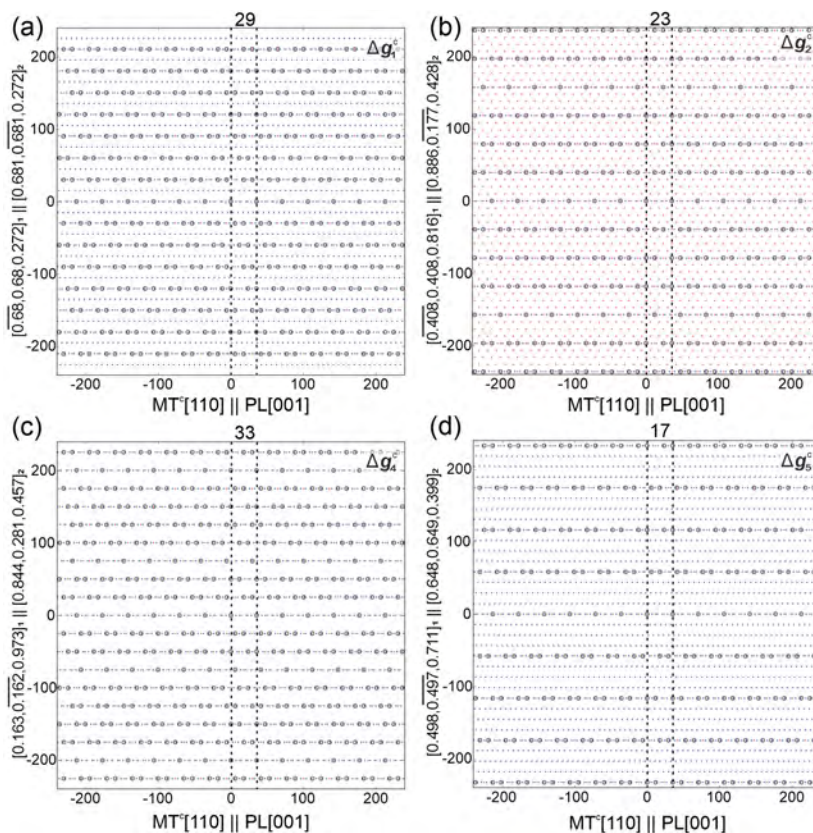


FIGURE 10. CCSL points (black circles) in the facet planes perpendicular to (a) Δg_1^f , (b) Δg_2^f , (c) Δg_3^f , and (d) Δg_5^f , as indicated at the top-right of each plot. The viewing direction is parallel to the respective Δg_i^f vector in each plot. The horizontal direction is the inclusion elongation direction. The red and blue spots represent lattice points of constrained magnetite (denoted as 1) and plagioclase (denoted as 2), the units are angstroms. The axes are labeled with the lattice directions of constrained magnetite (denoted as 1) and plagioclase (denoted as 2), the units are angstroms. The vertical dashed lines in each plot indicate the range of $[-0.1, 29.6] \text{ \AA}$ on the Z -axis, referred to as one repetition unit. The absolute numbers of the CCSL points within this range are indicated above each plot.

the other facets (Fig. 5b).

In the constrained situation $\Delta g_1^c \parallel \Delta g_6^c$, $\Delta g_2^c \parallel \Delta g_3^c$, and $\Delta g_4^c \parallel \Delta g_5^c$, the corresponding interface planes may account for an entire hexagonal needle cross-section bounded by three pairs of exact interfaces in the sense of Robinson et al. (1971). Upon relaxation of the constraint, a network of dislocations emerges that accommodates the resulting lattice misfit between magnetite and plagioclase (Ye and Zhang 2002). In general, the observed interface facets show minute deviations from the facets obtained for the constrained situation. Typically, the facets corresponding to exact interfaces in the constrained situation decompose into ledge and terrace associations in the actual configuration, where the terraces follow the orientation of the exact interface from the constrained situation, and the ledges account for the lattice mismatch. Interface facets F2 and F4 (Figs. 5e–5f) correspond to such configurations.

The iDPC-STEM image in Figure 5f shows that the F2 interface facet decomposed into nanometer-sized ledges and terraces. From the corresponding FFT result, the orientation of the terraces is parallel to the orientation of Δg_5^c , i.e., $MT(\bar{1}\bar{1}1) \parallel PL(150)$. In Figure 9d CCSL points in the vicinity of Δg_5^c are connected by a zigzag line, corresponding to terraces parallel to $MT(\bar{1}\bar{1}1) \parallel PL(150)$ and ledges parallel to F4. The averaged orientation of the zigzag line is nearly parallel to $PL(010)$, which is identical to the orientation obtained from the FFT of Figure 5f. The relative length of the ledge and terrace trace segments are consistent with the experimental results. Thus, we infer that the interface facet related to Δg_5^c transformed into a stepped structure containing ledge traces parallel to F4. We hypothesize that this transformation was driven by the tendency to increase the area density of CCSL points on the interface, which is higher for F4 interface planes than for the interface plane corresponding to Δg_5^c .

We suggest that the seven segments that bound the cross-section of the inclusion are derived from the four interface facets in the constrained configuration. The lattice mismatch at the magnetite-plagioclase interfaces is assumed to be accommodated by a network of dislocations (Ye and Zhang 2002). Even if the exact Burgers vectors of the dislocations remain unclear, the CCSL provides a reference for an idealized interface configuration and qualitatively explains the preference of certain facets.

Accommodation structures at interfaces of COR1B PL[001]-MT inclusions

The high-resolution iDPC-STEM images of the COR1B PL[001]-MT inclusion shown in Figure 6 reveal the close linkage between continuous layers composed of alternating tetrahedrally and octahedrally coordinated Fe atoms parallel to $MT(001)$ in magnetite to the columns parallel to the PL[001] in plagioclase across the magnetite-plagioclase interface. Apparently, along the magnetite-plagioclase interface, the spacing between the channels parallel to PL[001] in plagioclase and the spacing between the continuous layers of Fe atoms parallel $MT(001)$ in magnetite differ, and the misfit between the two structural elements in the crystal structures of magnetite and plagioclase leads to various accommodation structures along the interface. The subtlest mode of accommodation is the kinking of the layers of Fe atoms parallel $MT(001)$ in magnetite close to the magnetite-plagioclase

interface such as is seen at the bottom of Figure 6b. This kinking may develop into a more severe mode of accommodation by the introduction of stacking faults as can be seen in Figures 6a and 7. The two stacking faults seen in Figure 7 are parallel to two different $MT\{111\}$ lattice planes.

The cooperative displacement over $1/6[1\bar{1}\bar{2}]$ on the stacking fault parallel $MT(\bar{1}\bar{1}\bar{1})$ and over $1/6[\bar{1}\bar{1}\bar{2}]$ on the stacking fault parallel $MT(\bar{1}\bar{1}1)$ leads to an overall displacement of the magnetite bounded by the two stacking faults and the magnetite-plagioclase interface over $2/3[00\bar{1}]$. Based on the notion that these stacking faults are only observed in the immediate vicinity of the magnetite-plagioclase interfaces, it is hypothesized that they are introduced to accommodate the misfit between the magnetite and the plagioclase lattices and to allow for better linkup between the $MT(001)$ lattice planes and the six-membered rings representing the channels parallel to $PL[001]$ in the plagioclase. It is not clear, whether the stacking faults were formed during precipitate growth, or were introduced after growth to release local stress that may have accumulated during precipitate growth. Occurrence of the stacking faults only in the immediate vicinity of the magnetite-plagioclase interface rather suggests formation after precipitate growth. The observed stacking faults correspond to the prominent $MT\{111\}\langle 112\rangle$ glide system in magnetite, which may have been activated to release local stress. It must be noted that the overall displacement neither is contained in the stacking fault parallel $MT(\bar{1}\bar{1}\bar{1})$ nor is it contained in the stacking fault parallel $MT(\bar{1}\bar{1}1)$. This implies that an extra layer of oxygen and iron extending parallel to $MT(\bar{1}\bar{1}\bar{1})$ and an extra layer of oxygen and iron extending parallel to $MT(\bar{1}\bar{1}1)$ need to be introduced along the two stacking faults. Displacement of the magnetite domain bounded by the two stacking faults thus requires material redistribution within the magnetite.

Finally, in some places, accommodation of the lattice misfit appears to have produced fundamental changes of the crystal structure of magnetite so that a new phase has formed along an about 1 nm wide zone at the magnetite-plagioclase interface. There is no direct evidence, but circumstantial evidence suggests that this may also have involved diffusive material redistribution and stoichiometry change of the Fe-oxide phase.

IMPLICATIONS

Petrographic evidence suggests that the PL[001] magnetite micro-inclusions are of secondary nature in that they are formed by recrystallization from older generations of so-called plane normal type magnetite micro-inclusions during hydrothermal processing of the rocks. The transformation of plane normal magnetite micro-inclusions to PL[001] micro-inclusions changes the magnetic anisotropy of magnetite-bearing plagioclase, which needs to be considered during single-grain magnetic measurements on plagioclase.

Six COR variants between PL[001] magnetite micro-inclusions and the plagioclase host exist, and they are related to one another by rational crystallographic operations, indicating crystallographic control on the SOR and CORs of the PL[001] magnetite micro-inclusions with the plagioclase host. The microscopic interface configurations associated with the different orientation variants ensure low-energy configurations in microstructural equilibrium and low-energy barriers for nucleation and

growth of magnetite precipitates in plagioclase.

The inclusions are faceted, where the interface facets are parallel to low-index lattice planes in either magnetite or plagioclase, or the interfaces are stepped with the terraces of the steps parallel to low-index lattice planes of either magnetite or plagioclase. In this context, either a good fit between the oxygen lattices of the two phases or the parallel alignment of oxygen layers in magnetite and plagioclase appears to be the controlling factor. iDPC-STEM images also reveal linkup between important crystal structure units in plagioclase and in magnetite across the magnetite-plagioclase interfaces. In addition, they reveal accommodation features that shift marginal parts of magnetite grains relative to the bulk precipitate to arrive at a better fit between the two lattices. Locally magnetite seems to have lost its structure and potentially was transformed into another phase in the immediate vicinity of the magnetite-plagioclase interface. The geometry of the accommodation features makes it necessary to invoke redistribution of Fe and O along the magnetite-plagioclase interface.

The orientation of the interface facets between plagioclase, which is a framework silicate, and magnetite, an oxide with a close-packed oxygen sublattice, can be explained by the Δg method. The interface facets are oriented perpendicular to the Δg vectors that link the g -vectors of low-index lattice planes of magnetite and plagioclase in reciprocal space. The orientations of the interface facets only slightly deviate from the orientations of exact phase boundaries, which can be constructed if one of the lattices is slightly deformed. By this operation, a CCSL emerges, and exact magnetite-plagioclase phase boundaries parallel to low-index lattice planes in the CCSL are obtained. Even if the constrained configuration probably never existed physically, the CCSL lattice and the Δg method applied to the constrained configuration are viable models that explain the selection of interface facets. In the actual configuration, the deviation from exact phase boundaries is small and is accommodated by dislocations.

ACKNOWLEDGMENTS AND FUNDING

We thank the constructive suggestions provided by two reviewers. Editorial handling is gratefully acknowledged. Funding by the Austrian Science Foundation (FWF), Grant No. I 3998N29, and by the Russian Foundation for Basic Research (RFBR), Grant No. 18-55-14003 is gratefully acknowledged. We thank Alexey Pertsev for providing the dredged sample. FIB sample preparation was done in the Laboratory for scanning electron microscopy and focused ion beam applications, Faculty of Geosciences, Geography and Astronomy at the University of Vienna (Austria). Authors thank the European Regional Development Fund and the State of Brandenburg for the Themis Z TEM [part of the Potsdam Imaging and Spectral Analysis Facility (PISA)].

REFERENCES CITED

- Ageeva, O., Habler, G., Topa, D., Waitz, T., Li, C., Pertsev, A., Griffiths, T., Zhilicheva, O., and Abart, R. (2016) Plagioclase hosted Fe-Ti-oxide micro-inclusions in an oceanic gabbro-plagiogranite association from the Mid Atlantic ridge at 13°34' N. *American Journal of Science*, 316, 85–109, <https://doi.org/10.2475/02.2016.01>.
- Ageeva, O., Bian, G., Habler, G., Pertsev, A., and Abart, R. (2020) Crystallographic and shape orientations of magnetite micro-inclusions in plagioclase. *Contributions to Mineralogy and Petrology*, 175, 95, <https://doi.org/10.1007/s00410-020-01735-8>.
- Ageeva, O., Habler, G., Gilder, S.A., Schuster, R., Pertsev, A., Pilipenko, O., Bian, G., and Abart, R. (2022) Oriented magnetite inclusions in plagioclase: Implications for the anisotropy of magnetic remanence. *Geochemistry, Geophysics, Geosystems*, 23(2), e2021GC010272, <https://doi.org/10.1029/2021GC010272>.
- Bäro, G. and Gleiter, H. (1974) On the structure and migration of incoherent interphase boundaries between f.c.c. and b.c.c. Crystals. *Acta Metallurgica*, 22, 141–143, [https://doi.org/10.1016/0001-6160\(74\)90003-0](https://doi.org/10.1016/0001-6160(74)90003-0).
- Beltenev, V.E., Ivanov, V., Rozhdstvenskaya, I., Cherkashov, G., Stepanova, T., Shilov, V., Pertsev, A., Davydov, M., Egorov, I., Melekestseva, I., and others. (2007) A new hydrothermal field at 13°30' N on the Mid-Atlantic Ridge. *InterRidge News*, 16, 9–10.
- Beltenev, V.E., Ivanov, V., Rozhdstvenskaya, I., Cherkashev, G.A., Stepanova, T.V., Shilov, V.V., Davydov, M.P., Laiba, A.A., Kaylio, V., Narkevsky, E., and others. (2009) New data about hydrothermal fields on the Mid-Atlantic Ridge between 11°–14°N: 32nd Cruise of R/V Professor Logatchev. *InterRidge News*, 18, 13–17.
- Bian, G., Ageeva, O., Rečnik, A., Habler, G., and Abart, R. (2021) Formation pathways of oriented magnetite micro-inclusions in plagioclase from oceanic gabbro. *Contributions to Mineralogy and Petrology*, 176, 104, <https://doi.org/10.1007/s00410-021-01864-8>.
- Bollmann, W. and Nissen, H.-U. (1968) A study of optimal phase boundaries: The case of exsolved alkali feldspars. *Acta Crystallographica*, A24, 546–557, <https://doi.org/10.1107/S0567739468001178>.
- Borisevich, A.Y., Lupini, A.R., and Pennycook, S.J. (2006) Depth sectioning with the aberration-corrected scanning transmission electron microscope. *Proceedings of the National Academy of Sciences*, 103, 3044–3048, <https://doi.org/10.1073/pnas.0507105103>.
- Cheadle, M.J. and Gee, J.S. (2017) Quantitative Textural Insights into the Formation of Gabbro in Mafic Intrusions. *Elements*, 13, 409–414, <https://doi.org/10.2138/gselements.13.6.409>.
- Davis, K.E. (1981) Magnetite rods in plagioclase as the primary carrier of stable NRM in ocean floor gabbros. *Earth and Planetary Science Letters*, 55, 190–198, [https://doi.org/10.1016/0012-821X\(81\)90098-4](https://doi.org/10.1016/0012-821X(81)90098-4).
- Dunlop, D.J. and Özdemir, Ö. (2001) *Rock Magnetism: Fundamentals and Frontiers*, 596 p. Cambridge University Press.
- Escartín, J., Mével, C., Petersen, S., Bonnemains, D., Cannat, M., Andreani, M., Augustin, N., Bezos, A., Chavagnac, V., Choi, Y., and others. (2017) Tectonic structure, evolution, and the nature of oceanic core complexes and their detachment fault zones (13°20'N and 13°30'N, Mid Atlantic Ridge). *Geochemistry, Geophysics, Geosystems*, 18, 1451–1482, <https://doi.org/10.1002/2016GC006775>.
- Feinberg, J.M., Wenk, H.-R., Renne, P.R., and Scott, G.R. (2004) Epitaxial relationships of clinopyroxene-hosted magnetite determined using electron backscatter diffraction (EBSD) technique. *American Mineralogist*, 89, 462–466, <https://doi.org/10.2138/am-2004-2-328>.
- Feinberg, J.M., Harrison, R.J., Kasama, T., Dunin-Borkowski, R.E., Scott, G.R., and Renne, P.R. (2006a) Effects of internal mineral structures on the magnetic remanence of silicate-hosted titanomagnetite inclusions: An electron holography study. *Journal of Geophysical Research*, 111 (B12), <https://doi.org/10.1029/2006JB004498>.
- Feinberg, J.M., Wenk, H.-R., Scott, G.R., and Renne, P.R. (2006b) Preferred orientation and anisotropy of seismic and magnetic properties in gabbronorites from the Bushveld layered intrusion. *Tectonophysics*, 420, 345–356, <https://doi.org/10.1016/j.tecto.2006.03.017>.
- Fleet, M.E. (1981) The structure of magnetite. *Acta Crystallographica*, B37, 917–920, <https://doi.org/10.1107/S0567740881004597>.
- Fleet, M.E., Bilcox, G.A., and Barnett, R.L. (1980) Oriented magnetite inclusions in pyroxenes from the Grenville province. *Canadian Mineralogist*, 18, 89–99.
- Haider, M., Rose, H., Uhlemann, S., Schwan, E., Kabius, B., and Urban, K. (1998) A spherical-aberration-corrected 200kV transmission electron microscope. *Ultramicroscopy*, 75, 53–60, [https://doi.org/10.1016/S0304-3991\(98\)00048-5](https://doi.org/10.1016/S0304-3991(98)00048-5).
- Hirsch, P.B. (1977) *Electron Microscopy of Thin Crystals*, 563 p. Krieger.
- Hwang, S.-L., Shen, P., Chu, H.-T., and Yui, T.F. (2000) Nanometer-size a-PbO₂-type TiO₂ in garnet: A thermobarometer for ultrahigh-pressure metamorphism. *Science*, 288, 321–324, <https://doi.org/10.1126/science.288.5464.321>.
- Hwang, S.-L., Shen, P., Yui, T.-F., and Chu, H.-T. (2010) On the coherency-controlled growth habit of precipitates in minerals. *Journal of Applied Crystallography*, 43, 417–428, <https://doi.org/10.1107/S0021889810007454>.
- Hwang, S.-L., Shen, P., Chu, H.-T., Yui, T.-F., and Iizuka, Y. (2015) Origin of rutile needles in star garnet and implications for interpretation of inclusion textures in ultrahigh-pressure metamorphic rocks. *Journal of Metamorphic Geology*, 33, 249–272, <https://doi.org/10.1111/jmg.12119>.
- Hwang, S.-L., Shen, P., Chu, H.-T., Yui, T.-F., Iizuka, Y., and Schertl, H.-P. (2019) Rutile inclusions in garnet from a dissolution-reprecipitation mechanism. *Journal of Metamorphic Geology*, 37, 1079–1098, <https://doi.org/10.1111/jmg.12502>.
- Jin, L., Jia, C.-L., Lindfors-Vrejoiu, I., Zhong, X.-Y., Du, H.-C., and Dunin-Borkowski, R.E. (2016) Direct demonstration of a magnetic dead layer resulting from A-site cation inhomogeneity in a (La,Sr)MnO₃ epitaxial film system. *Advanced Materials Interfaces*, 3, 1600414, <https://doi.org/10.1002/admi.201600414>.
- Karson, J.A. and Lawrence, R.M. (1997) Tectonic setting of serpentinite exposures on the western median valley wall of the MARK area in the vicinity of Site 920. *Proceedings of the Ocean Drilling Program, Scientific Results*, 153, 5–22.
- Kent, D.V., Honnorez, B.M., Opydyke, N.D., and Fox, P.J. (1978) Magnetic properties of dredged oceanic gabbros and the source of marine magnetic anomalies. *Geophysical Journal International*, 55, 513–537, <https://doi.org/10.1111/j.1365->

- 246X.1978.tb05925.x.
- Knafelc, J., Filiberto, J., Ferré, E.C., Conder, J.A., Costello, L., Crandall, J.R., Dyar, M.D., Friedman, S.A., Hummer, D.R., and Schwenzer, S.P. (2019) The effect of oxidation on the mineralogy and magnetic properties of olivine. *American Mineralogist*, 104, 694–702, <https://doi.org/10.2138/am-2019-6829>.
- Koch, C.T. (2002) Determination of core structure periodicity and point defect density along dislocations. Ph.D. thesis, Arizona State University.
- Kogure, T. and Okunishi, E. (2010) Cs-corrected HAADF-STEM imaging of silicate minerals. *Journal of Electron Microscopy*, 59, 263–271, <https://doi.org/10.1093/jmicro/dfq003>.
- Krivanek, O.L., Dellby, N., and Lupini, A.R. (1999) Towards sub-Å electron beams. *Ultramicroscopy*, 78, 1–11, [https://doi.org/10.1016/S0304-3991\(99\)00013-3](https://doi.org/10.1016/S0304-3991(99)00013-3).
- Lazić, I., Bosch, E.G.T., and Lazar, S. (2016) Phase contrast STEM for thin samples: Integrated differential phase contrast. *Ultramicroscopy*, 160, 265–280, <https://doi.org/10.1016/j.ultramic.2015.10.011>.
- Li, C., Griffiths, T., Pennycook, T.J., Mangler, C., Jeřábek, P., Meyer, J., Habler, G., and Abart, R. (2016) The structure of a propagating MgAl₂O₄/MgO interface: Linked atomic- and μm-scale mechanisms of interface motion. *Philosophical Magazine*, 96, 2488–2503, <https://doi.org/10.1080/14786435.2016.1205233>.
- Luo, C.P. and Weatherly, G.C. (1988) The interphase boundary structure of precipitates in a Ni-Cr alloy. *Philosophical Magazine. A. Physics of Condensed Matter. Defects and Mechanical Properties*, 58, 445–462, <https://doi.org/10.1080/01418618808210423>.
- MacLeod, C.J., Searle, R.C., Murton, B.J., Casey, J.F., Mallows, C., Unsworth, S.C., Achenbach, K.L., and Harris, M. (2009) Life cycle of oceanic core complexes. *Earth and Planetary Science Letters*, 287, 333–344, <https://doi.org/10.1016/j.epsl.2009.08.016>.
- Nikolaissen, E.S., Harrison, R., Fabian, K., Church, N., McEnroe, S.A., Sørensen, B.E., and Tegner, C. (2022) Hysteresis parameters and magnetic anisotropy of silicate-hosted magnetite exsolutions. *Geophysical Journal International*, 229, 1695–1717, <https://doi.org/10.1093/gji/ggac007>.
- Ondréas, H., Cannat, M., Fouquet, Y., and Normand, A. (2012) Geological context and vents morphology of the ultramafic-hosted Ashadze hydrothermal areas (Mid-Atlantic Ridge 13°N). *Geochemistry, Geophysics, Geosystems*, 13, 2012GC004433, <https://doi.org/10.1029/2012GC004433>.
- Pennycook, S.J. (2017) The impact of STEM aberration correction on materials science. *Ultramicroscopy*, 180, 22–33, <https://doi.org/10.1016/j.ultramic.2017.03.020>.
- Pertsev, A.N., Bortnikov, N.S., Vlasov, E.A., Beltenev, V.E., Dobretsova, I.G., and Ageeva, O.A. (2012) Recent massive sulfide deposits of the Semenov ore district, Mid-Atlantic Ridge, 13°31'N: Associated rocks of the oceanic core complex and their hydrothermal alteration. *Geology of Ore Deposits*, 54, 334–346, <https://doi.org/10.1134/S1075701512050030>.
- Pertsev, A.N., Aranovich, L.Y., Prokofiev, V.Y., Bortnikov, N.S., Cipriani, A., Simakin, S.S., and Borisovskiy, S.E. (2015) Signatures of residual melts, magmatic and seawater-derived fluids in Oceanic Lower-Crust Gabbro from the Vema Lithospheric Section, Central Atlantic. *Journal of Petrology*, 56, 1069–1088, <https://doi.org/10.1093/petrology/egv028>.
- Proyer, A., Habler, G., Abart, R., Wirth, R., Krenn, K., and Hoinkes, G. (2013) TiO₂ exsolution from garnet by open-system precipitation: Evidence from crystallographic and shape preferred orientation of rutile inclusions. *Contributions to Mineralogy and Petrology*, 166, 211–234, <https://doi.org/10.1007/s00410-013-0872-7>.
- Renne, P.R., Scott, G.R., Glen, J.M.G., and Feinberg, J.M. (2002) Oriented inclusions of magnetite in clinopyroxene: Source of stable remanent magnetization in gabbros of the Messum Complex, Namibia. *Geochemistry, Geophysics, Geosystems*, 3, 1–11, <https://doi.org/10.1029/2002GC000319>.
- Robinson, P., Jaffe, H.W., Ross, M., and Klein, C. Jr. (1971) Orientation of exsolution lamellae in clinopyroxenes and clin amphiboles: Consideration of optimal phase boundaries. *American Mineralogist*, 56, 909–939.
- Selkin, P.A., Gee, J.S., and Meurer, W.P. (2014) Magnetic anisotropy as a tracer of crystal accumulation and transport, Middle Banded Series, Stillwater Complex, Montana. *Tectonophysics*, 629, 123–137, <https://doi.org/10.1016/j.tecto.2014.03.028>.
- Shi, Z.-Z., Dai, F.-Z., Zhang, M., Gu, X.-F., and Zhang, W.-Z. (2013) Secondary coincidence site lattice model for truncated triangular β-Mg₂Sn precipitates in a Mg-Sn-based alloy. *Metallurgical and Materials Transactions. A, Physical Metallurgy and Materials Science*, 44, 2478–2486, <https://doi.org/10.1007/s11661-013-1633-y>.
- Shi, Z.-Z., Chen, H.-T., Zhang, K., Dai, F.-Z., and Liu, X.-F. (2021) Crystallography of precipitates in Mg alloys. *Journal of Magnesium and Alloys*, 9, 416–431, <https://doi.org/10.1016/j.jma.2020.06.013>.
- Sobolev, P.O. (1990) Orientation of acicular iron-ore mineral inclusions in plagioclase. *International Geology Review*, 32, 616–628, <https://doi.org/10.1080/00206819009465804>.
- Sutton, A.P. and Balluffi, R.W. (1995) *Interfaces in Crystalline Materials*, 856 p. Oxford University Press.
- Tan, W., Liu, P., He, H., Wang, C.Y., and Liang, X. (2016) Mineralogy and origin of exsolution in Ti-rich magnetite from different magmatic Fe-Ti oxide-bearing intrusions. *Canadian Mineralogist*, 54, 539–553, <https://doi.org/10.3749/canmin.1400069>.
- Usui, Y., Shibuya, T., Sawaki, Y., and Komiya, T. (2015) Rock magnetism of tiny exsolved magnetite in plagioclase from a Paleoproterozoic granitoid in the Pilbara craton. *Geochemistry, Geophysics, Geosystems*, 16, 112–125, <https://doi.org/10.1002/2014GC005508>.
- Wager, L.R. and Mitchell, R.L. (1951) The distribution of trace elements during strong fractionation of basic magma—A further study of the Skaergaard intrusion, East Greenland. *Geochimica et Cosmochimica Acta*, 1, 129–208, [https://doi.org/10.1016/0016-7037\(51\)90016-6](https://doi.org/10.1016/0016-7037(51)90016-6).
- Wenk, H.R., Joswig, W., Tagai, T., Korekawa, M., and Smith, B.K. (1980) The average structure of An_{62–66} labradorite. *American Mineralogist*, 65, 81–95.
- Wenk, H.-R., Chen, K., and Smith, R. (2011) Morphology and microstructure of magnetite and ilmenite inclusions in plagioclase from Adirondack anorthositic gneiss. *American Mineralogist*, 96, 1316–1324, <https://doi.org/10.2138/am.2011.3760>.
- Ye, F. and Zhang, W.-Z. (2002) Coincidence structures of interfacial steps and secondary misfit dislocations in the habit plane between Widmanstätten cementite and austenite. *Acta Materialia*, 50, 2761–2777, [https://doi.org/10.1016/S1359-6454\(02\)00077-0](https://doi.org/10.1016/S1359-6454(02)00077-0).
- Yücelen, E., Lazić, I., and Bosch, E.G.T. (2018) Phase contrast scanning transmission electron microscopy imaging of light and heavy atoms at the limit of contrast and resolution. *Scientific Reports*, 8, 2676, <https://doi.org/10.1038/s41598-018-20377-2>.
- Zhang, W.-Z. (2020) Reproducible orientation relationships developed from phase transformations—Role of interfaces. *Crystals*, 10, 1042, <https://doi.org/10.3390/cryst10111042>.
- Zhang, W.-Z. and Purdy, G.R. (1993) O-lattice analyses of interfacial misfit. I. General considerations. *Philosophical Magazine. A. Physics of Condensed Matter. Defects and Mechanical Properties*, 68, 279–290, <https://doi.org/10.1080/01418619308221205>.
- Zhang, W.-Z. and Weatherly, G.C. (2005) On the crystallography of precipitation. *Progress in Materials Science*, 50, 181–292, <https://doi.org/10.1016/j.pmatsci.2004.04.002>.
- Zhang, W.-Z. and Yang, X.-P. (2011) Identification of singular interfaces with Ags and its basis of the O-lattice. *Journal of Materials Science*, 46, 4135–4156, <https://doi.org/10.1007/s10853-011-5431-x>.

MANUSCRIPT RECEIVED SEPTEMBER 7, 2022

MANUSCRIPT ACCEPTED FEBRUARY 9, 2023

ACCEPTED MANUSCRIPT ONLINE FEBRUARY 16, 2023

MANUSCRIPT HANDLED BY LINDSAY P. KELLER

Endnote:

¹Deposit item AM-23-98784. Online Materials are free to all readers. Go online, via the table of contents or article view, and find the tab or link for supplemental materials.